iScience

CellPress

Article

The RNA Processing Factor Y14 Participates in DNA Damage Response and Repair

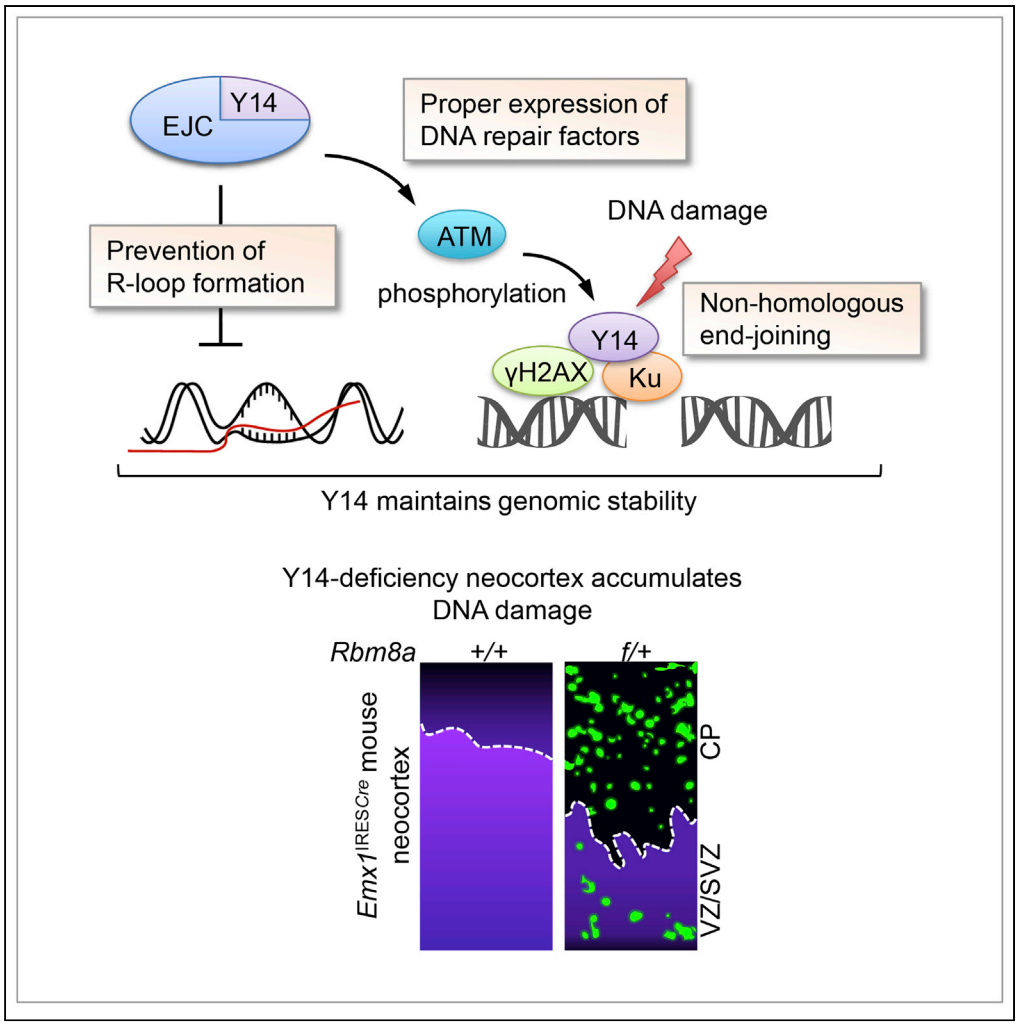

Tzu-Wei Chuang, Chia-Chen Lu, Chun-Hao Su, ..., Kuo-Ming Lee, Ching-Yen Tsai, Woan-Yuh Tarn

wtarn@ibms.sinica.edu.tw

HIGHLIGHTS

Y14 deficiency leads to DNA damage accumulation

Y14 depletion disturbs DNA damage response and induces R-loops

Y14 promotes Ku70/80 recruitment to DNA damage sites

Y14 participates in DNA damage repair

Chuang et al., iScience *13*, 402–415
March 29, 2019
https://doi.org/10.1016/j.isci.2019.03.005

iScience

CellPress

Article

The RNA Processing Factor Y14 Participates in DNA Damage Response and Repair

Tzu-Wei Chuang,[1,6] Chia-Chen Lu,[1,2,6] Chun-Hao Su,[1,6] Pei-Yu Wu,[3] Sarasvathi Easwvaran,[1] Chi-Chieh Lee,[1] Hung-Che Kuo,[1] Kuan-Yang Hung,[1] Kuo-Ming Lee,[1,5] Ching-Yen Tsai,[4] and Woan-Yuh Tarn[1,7,*]

SUMMARY

DNA repair deficiency leads to genome instability and hence human disease. Depletion of the RNA processing factor Y14/RBM8A in cultured cells or *Rbm8a* haplodeficiency in the developing mouse cortex results in the accumulation of DNA damage. Y14 depletion differentially affected the expression of DNA damage response (DDR) factors and induced R-loops, both of which threaten genomic stability. Immunoprecipitation coupled with mass spectrometry revealed DDR factors as potential Y14-interacting partners. Further results confirmed that Y14 interacts with Ku and several DDR factors in an ATM-dependent manner. Y14 co-fractionated with Ku in chromatin-enriched fractions and further accumulated on chromatin upon DNA damage. Y14 knockdown delayed recruitment of DDR factors to DNA damage sites and formation of γH2AX foci and also led to Ku retention on chromatin. Accordingly, Y14 depletion compromised the efficiency of DNA end joining. Therefore Y14 likely plays a direct role in DNA damage repair via its interaction with DDR factors.

INTRODUCTION

Genome stability can be threatened by a variety of DNA lesions, which may result from exogenous DNA-damaging agents or endogenous causes such as DNA repair factor dysfunction or oxidative stress. Failure to repair DNA damage leads to a wide spectrum of human diseases and developmental disorders (Jackson and Bartek, 2009). Cellular response to DNA damage is initiated by damage recognition followed by complex signaling cascades that determine repair mechanisms, and ultimately, DNA repair factors are recruited to damaged sites for DNA repair (Chapman et al., 2012).

Double-strand breaks (DSBs) are one of the most deleterious DNA lesions. DSB repair essentially involves homologous recombination or non-homologous end joining (NHEJ), which require overlapping but distinct sets of DNA repair factors (Chapman et al., 2012). Homologous recombination is more prevalent during cell cycle phases S and G2, whereas NHEJ is active throughout the entire cell cycle and thus constitutes one of the major DNA repair pathways (Chapman et al., 2012). The sensor complexes, Mre11/Rad50/Nbs1 (MRN) and Ku70/Ku80 (abbreviated Ku70/80), recognize DSB ends and recruit respective DNA damage response (DDR) and repair factors. In NHEJ, the complex of Ku70/80 and DNA-dependent protein kinase (DNA-PK) recruits the end-processing ligation complex containing XLF, XRCC4, and DNA ligase IV, which rejoins broken ends. In addition, DDR signaling may activate cell cycle checkpoints or apoptosis.

Accumulating evidence indicates that RNA processing factors contribute both directly and indirectly to genome stability (Naro et al., 2015; Wickramasinghe and Venkitaraman, 2016). Several splicing factors modulate alternative splicing of DDR or apoptosis factors (Shkreta and Chabot, 2015). Depletion of RNA processing factors results in the formation of R-loops that are prone to DNA damage (Santos-Pereira and Aguilera, 2015). Moreover, RNA processing factors may have a direct role in DNA repair via their interactions with DNA repair factors (Naro et al., 2015; Wickramasinghe and Venkitaraman, 2016). Some of these RNA processing factors are recruited to DNA damage sites in a manner that is dependent on DDR-kinase-mediated phosphorylation or poly-ADP ribosylation. Recent reports indicate the intriguing role of RNA molecules in DNA damage repair (Hawley et al., 2017). Therefore a set of RNA processing factors may participate in small RNA biogenesis around DSBs or coordinate with non-coding RNAs in DDR. These findings underscore the importance of RNA-processing-mediated DNA repair.

The RNA processing factor Y14, encoded by *Rbm8a*, plays multiple roles in mRNA metabolism. Essentially, Y14 acts as a core factor of the exon-junction complex (EJC), which is involved in nonsense-mediated

[1]Institute of Biomedical Sciences, Academia Sinica, 128 Academy Road Section 2, Nankang, Taipei 11529, Taiwan

[2]Taiwan International Graduate Program in Molecular Medicine, National Yang-Ming University and Academia Sinica, Taipei, Taiwan

[3]Institute of Biochemistry, Academia Sinica, Taipei, Taiwan

[4]Institute of Molecular Biology, Academia Sinica, Taipei, Taiwan

[5]Present address: Research Center for Emerging Viral Infections, College of Medicine, Chang Gung University, Taoyuan, Taiwan

[6]These authors contributed equally

[7]Lead Contact

*Correspondence: wtarn@ibms.sinica.edu.tw

https://doi.org/10.1016/j.isci.2019.03.005

mRNA decay and mRNA translation (Chuang et al., 2015). The EJC components, including Y14, also participate in alternative splicing of apoptosis factors, of which the spliced isoforms have opposing functions in apoptosis (Michelle et al., 2012; Wang et al., 2014; Fukumura et al., 2016). Y14 depletion in general induces a switch to pro-apoptotic isoforms and leads to cell death. Mouse genetic studies show that Y14 is critical for embryonic cortical development (Mao et al., 2015, 2016). *Rbm8a* haploinsufficiency in mouse embryonic brain causes cell death and reduces the number of neural progenitors and neurons. Depletion of Y14 in cultured cells increases the number of sub-G1 phase cells and ultimately leads to apoptosis (Ishigaki et al., 2013; Lu et al., 2017). Moreover, Y14-depleted cells spontaneously accumulate DSBs and exhibit hypersensitivity to DNA-damaging agents (Lu et al., 2017). Therefore, we attempted to explore the potential role of Y14 in the maintenance of genome integrity. We uncovered the interaction of Y14 with DNA damage repair factors and demonstrated its unprecedented role in DNA damage repair and DDR signaling.

RESULTS

Y14 Depletion Results in Cumulative DNA Damage and Reduced Cell Viability and Proliferation Capacity

We previously showed that Y14 depletion increases the level of phosphorylated H2AX (γH2AX) and apoptosis in HeLa cells (Lu et al., 2017). HeLa cells exhibit diminished p53 function, and depletion of Y14 by small interfering RNA (siRNA)-induced p53β, a splice isoform of p53, to a great extent (Lu et al., 2017; Figure 1A, lane 2). We therefore evaluated the aforementioned aspects using human osteosarcoma U2OS cells, which express functional p53 and exhibited only a minimal level of p53β upon Y14 depletion (Figure 1A, lane 4). Y14 depletion consistently increased the level of γH2AX in both cell lines, although U2OS had a lower basal γH2AX level (Figure 1A). This observation was consistent with immunofluorescence, which shows a higher background level of γH2AX foci in HeLa cells than U2OS cells. Y14 depletion, nevertheless, increased the signal of γH2AX foci in both cells (Figure S1). Clonogenic assay revealed that Y14 depletion significantly reduced survival of both cell lines (Figure 1B). Therefore, Y14-depletion-induced DNA damage and cell growth inhibition may be irrespective of p53 status.

Meanwhile, we assessed Y14-depletion-induced DNA damage in animal models. It has been reported that *Rbm8a* haploinsufficiency causes apoptosis of neural progenitor cells in the embryonic cerebral cortex (Mao et al., 2015). We speculated that Y14-deficient neocortex has accumulative DNA damage, which leads to cell death. To test this hypothesis, we generated $Rbm8a^{f/+}$ mice (Supplemental Information) as previously reported (Mao et al., 2015), for which *loxP* insertion was confirmed by genotyping and sequencing (Figures S2A and S2B). $Rbm8a^{f/+}$ mice were mated with $Emx1^{IREScre}$ mice (Gorski et al., 2002) to generate $Emx1^{IREScre}$;$Rbm8a^{f/+}$. Immunoblotting of $Emx1^{IREScre}$;$Rbm8a^{f/+}$ cortical plates at embryonic day (E) 13.5 revealed reduced Y14 expression (Figure S2C). As reported (Mao et al., 2015), the $Emx1^{IREScre}$;$Rbm8a^{f/+}$ brain at postnatal day 10 exhibited microcephaly compared with their littermate controls (Figure S2D). This *Rbm8a* haploinsufficiency significantly increased the level of γH2AX and activated caspase 3 (CC3) in the neocortex at E13.5 (Figures 1C and S2E, respectively). Immunostaining of dissociated cell cultures of the E13.5 neocortex showed an ~50% reduction of Pax6-positive radial glia cells in $Emx1^{IREScre}$;$Rbm8a^{f/+}$ (Figure S2F), as reported (Mao et al., 2015). Nevertheless, higher levels of γH2AX and CC3 were detected in the remaining Pax6-positive cells (Figures 1D and S2G upper for γH2AX, and Figures 1E and S2G lower for CC3). Accordingly, *Rbm8a* haploinsufficiency impaired the expansion of neural stem or progenitor cells to form neurospheres (Figure 1F), which might have in part resulted from accumulated DNA damage and cell apoptosis. Together, we provided evidence from both cultured cells and animal models for the role of Y14 in genome stability. Y14 deficiency has a detrimental effect on cell viability and neural stem cell proliferation.

Y14 Depletion Causes DNA Damage, Perturbs the DDR, and Induces R-Loops

To quantify DNA damage in Y14-depleted cells, we performed the neutral comet assay. The result showed that Y14 depletion generated fragmented DNA, i.e., comet tail, in HeLa cells even without ionizing radiation (IR) treatment (Figure 2A). Y14-depleted MCF7 and U2OS cells exhibited different levels of DNA damage (Figure S3A), which may reflect their different repair or tolerance capacities. IR treatment caused an increase in olive tail moment in both control and Y14-depleted HeLa cells, but the latter exhibited a significantly higher level of DNA damage after IR (Figure 2B). Consistently, IR treatment reduced cell viability of both HeLa and U2OS cells (Figure S3B), indicating that Y14 loss increased cell sensitivity to DNA damage.

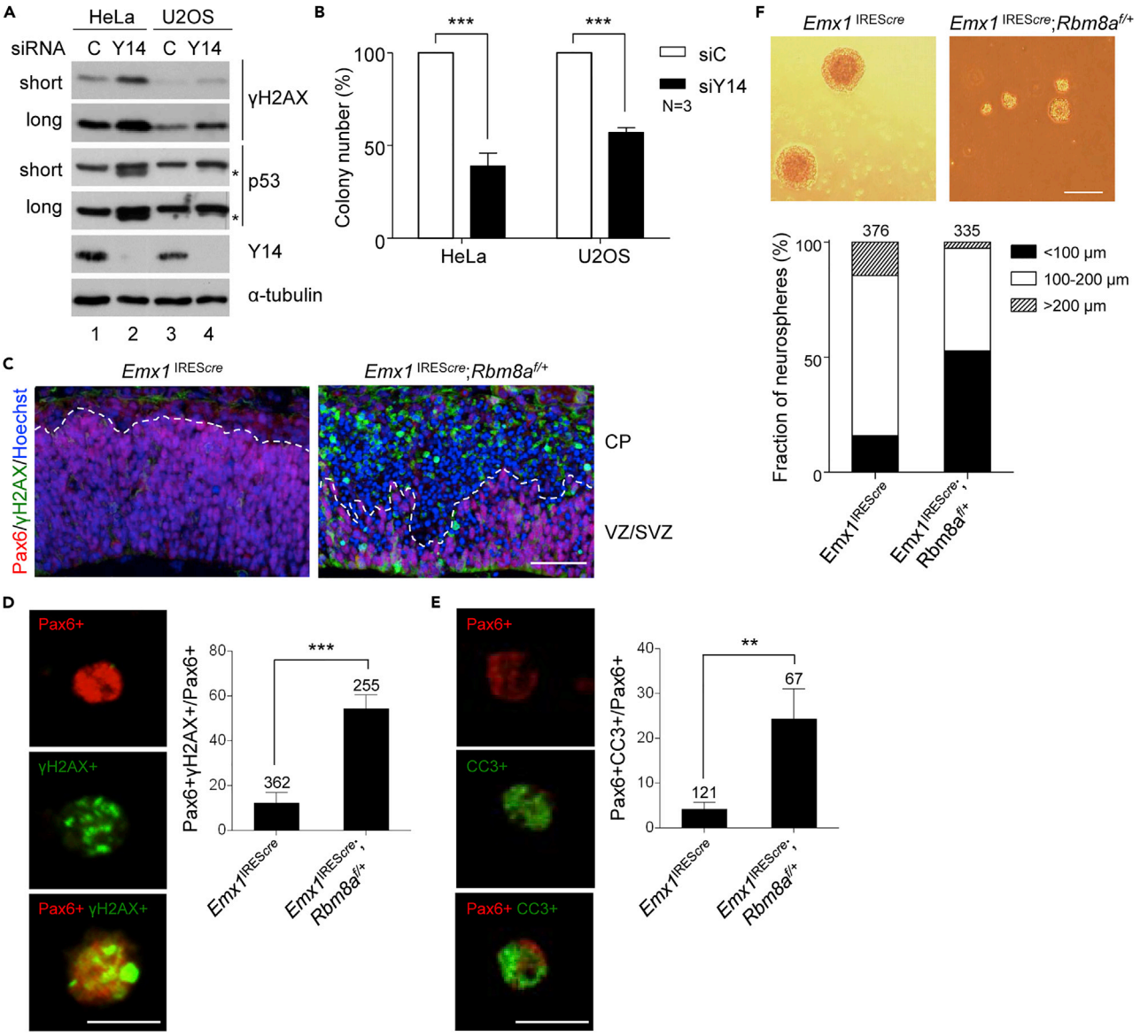

Figure 1. Y14 Deficiency Results in Cumulative DNA Damage, Reduced Cell Viability, and Impaired Neurosphere Formation

(A) HeLa and U2OS cells were transfected with control siRNA (siC) or siY14. Immunoblotting shows γH2AX and p53 in both short and long exposures and Y14 and α-tubulin. Asterisk indicates p53β.

(B) Clonogenic assay was performed in siRNA-transfected HeLa and U2OS cells. The bar graph shows relative colony-forming units (percentage; mean ± SD). N indicates the number of replicates.

(C) E13.5 dorsal neocortices of *Emx1*^{IREScre} and *Emx1*^{IREScre};*Rbm8a*$^{f/+}$ mice were subjected to immunostaining using antibodies against γH2AX and Pax6 and Hoechst staining. Dashed line indicates the boundary of the ventricular zone/subventricular zone (VZ/SVZ) and the cortical plate (CP). Scale bar, 50 μm.

(D) Primary cells dissociated from the dorsal neocortices as in (C) were subjected to immunostaining using antibodies against Pax6 and γH2AX as well as Hoechst staining (also see Figure S2F). Representative magnified images show Pax6+, γH2AX+, and double-positive cells of *Emx1*^{IREScre};*Rbm8a*$^{f/+}$ without Hoechst staining. Scale bar in , 10 μm in (D and E). Bar graphs show percentage of γH2AX+ cells among Pax6+ cells (mean ± SD). (D–F) The number of cells analyzed is indicated above the bars; cells were obtained from three pairs of littermates.

(E) As in (D), immunostaining was performed using anti-Pax6 and anti-cleaved caspase 3 (CC3) (also see Figure S1G). Representative magnified images show Pax6+, CC3+, and double-positive cells. Bar graphs show percentage of CC3+ cells among Pax6+ cells (mean ± SD).

(F) Neurosphere formation was performed using dissociated cells from E13.5 dorsal neocortices as in (C) (scale bar, 200 μm). Stacked bar graph shows percentage of different sizes (<100 μm, 100–200 μm, and >200 μm) of neurospheres.

In all bar graphs of Figures 1, 2, 3, 4, 5, 6, and 7, p values are as follows: *p < 0.05, **p < 0.01, ***p <0.001.

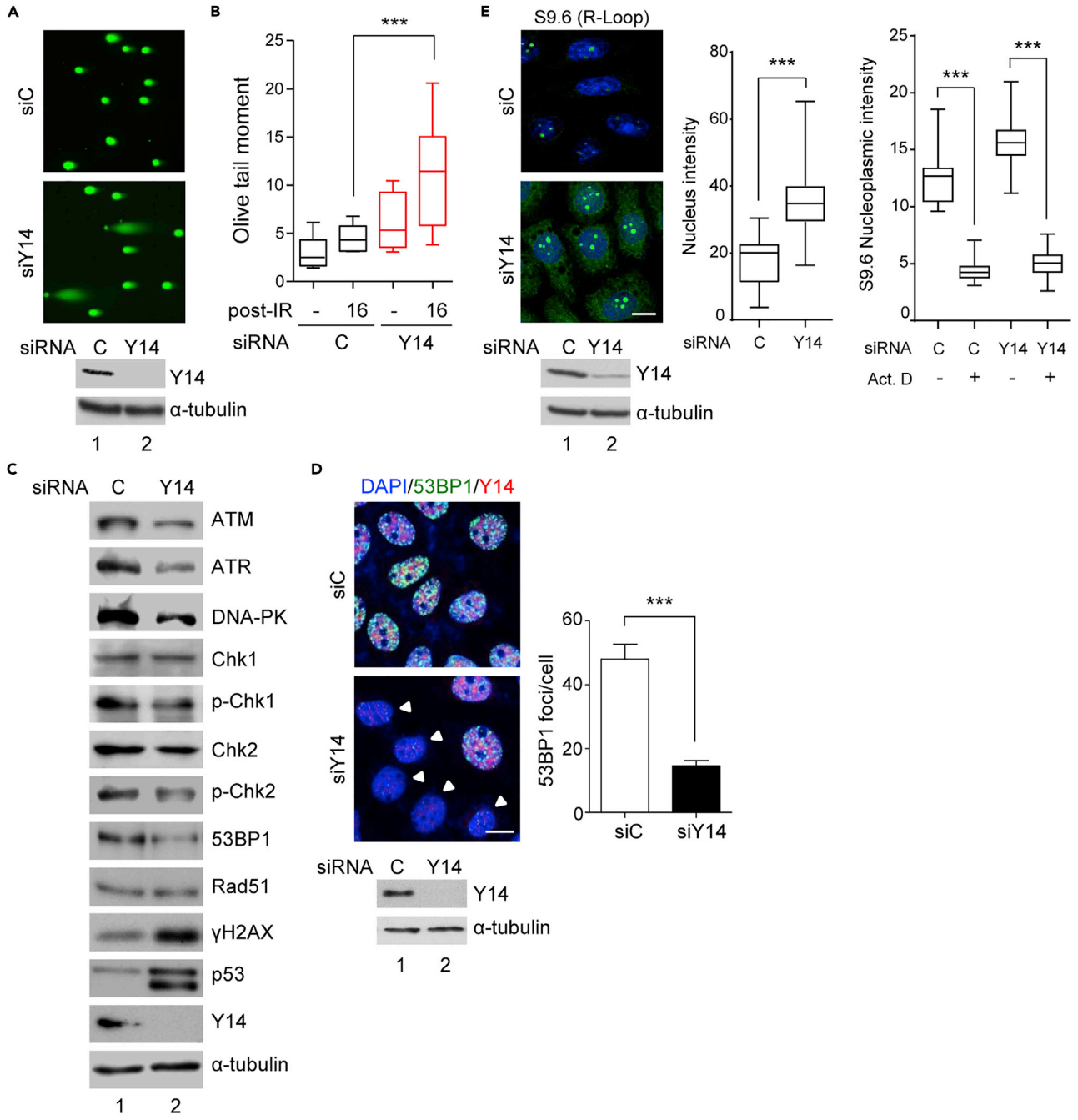

Figure 2. Y14 Depletion Causes DNA Damage, Induces R-Loops, and Perturbs DDR

(A) The comet assay of siRNA-transfected HeLa cells. Immunofluorescence shows SYBR Green staining of DNA. (A, C, and E) Immunoblotting shows Y14 and α-tubulin.

(B) siRNA-transfected HeLa cells as in (A) were either not treated (−) or treated with 2 Gy IR followed by 16-h recovery. Box and whiskers plot shows the comet tail moment; mean ± SD were from ~300 cells in three independent experiments.

(C) Immunoblotting of siC- or siY14-transfected HeLa cell lysates was performed using antibodies against the indicated proteins.

(D) siRNA-transfected HeLa cells were treated with 10 Gy IR followed by recovery for 30 min. Immunofluorescence was performed using anti-53BP1 and anti-Y14. Arrowheads, Y14-depleted cells. Scale bar, 10 μm. The number (mean ± SD) of 53BP1 foci per cell is shown in the bar graph; ~200 cells were counted in three independent experiments.

(E) siRNA-transfected HeLa cells were subjected to immunofluorescence using antibody S9.6; the images were merged with DAPI staining (scale bar, 10 μm). Box and whiskers plot shows quantification of nuclear (left) and mock or actinomycin D-treated nucleolus-excluding nucleoplasmic (right) S9.6 signals. For each transfection, ~100 cells were scored from three independent experiments.

Y14 depletion differentially affects gene expression (Michelle et al., 2012; Wang et al., 2014; Fukumura et al., 2016; Lu et al., 2017). Therefore we examined the expression of a panel of DDR signaling factors in Y14-depleted HeLa cells. Immunoblotting showed that Y14 depletion induced p53β and γH2AX, as previously reported (Lu et al., 2017) and reduced the level of three major upstream DDR kinases, namely, ATM, ATR, and DNA-PK (Figure 2C). A similar result was obtained in Y14-depleted MCF7 and U2OS cells (Figure S4A). Moreover, a reduction in the phosphorylation level of the two checkpoint kinases, Chk1 and Chk2, in Y14-depleted HeLa cells supported defective DDR signaling (Figure 2C). In addition, we observed that the level of 53BP1, but not Rad51, was also reduced in Y14-depleted cells (Figures 2C and S4A). Immunofluorescence further indicated the reduction in IR-induced 53BP1 foci in Y14-depleted HeLa cells (Figure 2D).

R-loops are RNA-DNA hybrids that form naturally during transcription and can act as a source of genomic instability (Santos-Pereira and Aguilera, 2015). Using immunofluorescence with antibody S9.6, we observed that Y14 depletion enhanced R-loop signals in both the nucleus and the cytoplasm (Figure 2E, HeLa; Figure S5A, MCF7 and U2OS cells). Dot blot analysis confirmed that the R-loop signal was increased by ~1.7-fold upon Y14 depletion and diminished after treatment with RNase H (Figure S5B). Although R-loops were abundant in the nucleoli, the nucleoplasmic R-loop signal was still visibly increased (Figures 2E and S5C for the images without DAPI staining). Such a signal was reduced by actinomycin D treatment (Figures S5C, and 2E, bar graph at the right), suggesting that R-loops form in a transcription-dependent manner. Overexpression of RNase H1 reduced γH2AX foci in Y14-depleted HeLa cells (Figure S5D), as observed in SRSF2-depleted cells (Sridhara et al., 2017), suggesting that R-loops contribute to Y14-deficiency-induced DNA damage. A DNA-RNA immunoprecipitation (DRIP)-coupled quantitative PCR (qPCR) analysis has previously shown that silencing of BRCA2 or THOC1 promotes R-loop accumulation at actively transcribed genes (Bhatia et al., 2014). Using DRIP-qPCR, we observed that Y14 depletion similarly increased R-loops in several transcriptionally active genes tested, including *Egr1*, *Apoe*, and *Rpl13A*, but not significantly in *Btdb19* and an intergenic negative control (Figure S5E). Our results thus indicated a potential role for Y14 in preventing co-transcriptional R-loop formation. Together, Y14 deficiency likely causes DNA damage, compromises DDR, and induces R-loops, all of which can lead to genome instability.

As Y14 is a part of the EJC, we also evaluated the effect of eIF4A3. Indeed, depletion of eIF4A3 caused DNA damage, downregulated several DDR proteins, and induced R-loops, as observed in Y14 depletion (Figures S3C, S4B, and S5F). This result was not unexpected, because it is well recognized that RNA processing factors contribute to genome stability via different mechanisms (Naro et al., 2015; Shkreta and Chabot, 2015; Wickramasinghe and Venkitaraman, 2016). However, whether Y14 and eIF4A3 function independently or inter-dependently in such events remains to be determined.

Y14 Interacts with DNA Damage Repair Factors

To explore the mechanism of Y14 depletion-induced DNA damage, we performed immunoprecipitation in combination with mass spectrometry using overexpressed FLAG-Y14 in HEK293 cells. Y14 co-precipitated proteins included the components of the EJC, the methylosome, the transcription factor/nuclear export (THOC) complexes, splicing factors, and ribosomal proteins, consistent with previous reports (reviewed in Chuang et al., 2015) (Table S1). Moreover, we identified a set of proteins implicated in DNA repair, including Ku70/80, Trim28, and Rad23a (Table 1). We first focused on the heterodimeric Ku complex owing to its prominent function in DSB repair and the maintenance of genomic stability (Jackson and Bartek, 2009). Immunoprecipitation of FLAG-Y14 followed by immunoblotting confirmed the interaction between Y14 with Ku70/80 and Trim28 as well as the DNA damage sensor and signaling factors (such as the MRN complex, MDC1, and γH2AX) and Ku-associated NHEJ factors (XRCC4, XLF, and DNA ligase IV) (Figure 3A, lane 5). We also demonstrated the interaction between endogenous Y14 and Ku80 (Figure 3B). However, eIF4A3, TAP, or Upf3b could not interact with Ku (Figures 3A, lane 6; S6A), emphasizing the specific interaction between Y14 and Ku.

Next, we characterized the nature of the interaction between Y14 and Ku. Intriguingly, the Y14-Ku interaction was completely disrupted by RNase treatment regardless of DNA damage (Figures 3C and S6B). Moreover, DNA damage did not particularly enhance their interaction (Figure 3D, lane 11). Inhibition of the DDR kinase ATM by KU55933, however, abolished the interaction of Y14 with Ku and γH2AX (Figure 3D, lane 12). Similar result was observed by depletion of ATM using siRNA (Figure S6C). ATM inactivation appeared to abolish the phosphorylation of overexpressed Y14 (Figure S6D). The C-terminal arginine/serine dipeptides

Protein Name	Accession No.	Peptide No.	Function
Ku80	P13010	5	DSB repair
Ku70	P12956	3	DSB repair
BRCA2	P51587	3	DNA damage repair
Trim28	Q13263	3	Transcriptional regulation DNA damage repair
RFC2	P35250	3	Replication factor
MCM8	Q9UJA3	2	DNA replication licensing factor
MCM10	Q7L590	2	DNA replication licensing factor
Rad23a	P54725	1	Nucleotide excision repair
RFC3	P40938	1	Replication factor

Table 1. Identification of Y14-interacting Proteins Implicated in DNA Damage Response, Repair, and Metabolism

are the major phosphorylation of Y14 in cells (Hsu Ia et al., 2005). To evaluate the effect of this C-terminal phosphorylation on the Y14-Ku interaction, we performed an *in vitro* pull-down assay using recombinant glutathione-*S*-transferase-Y14 fusion as bait. The result showed that full-length unphosphorylated Y14 could interact with Ku80, albeit barely, and, nevertheless, the C-terminal region was critical for the interaction (Figure 3E, lanes 4 and 5). Strikingly, phosphorylation of Y14 (see Transparent Methods) greatly enhanced its interaction with Ku70/80 (lane 6), supporting the observation in cells. Finally, we evaluated the interaction between Y14 and Trim28, which functions in both transcription and DNA repair (Bunch and Calderwood, 2015). We observed that the transcription inhibitor DRB disrupted the interaction of Y14 with RNA polymerase II (RNA pol II) and Trim28, but not γH2AX (Figure 3F), suggesting that the Y14-Trim28 interaction is more likely involved in transcriptional regulation.

Together, our results revealed an EJC-independent but RNA-dependent interaction of Y14 with Ku, and, moreover, suggested a positive feedback loop between Y14 and DDR signaling factors, which likely promotes genome stability (Figure 3G and see Discussion).

Y14 Associates with Chromatin and Further Accumulates on Chromatin after DNA Damage

Next, we accessed subnuclear localization of Y14 and Ku by fractionation of HeLa cell lysates (Brown et al., 2015). The result showed that Y14, but not eIF4A3 or Magoh, co-fractionated with Ku70/80 in the chromatin-enriched fraction (Figure 4A, lane 2). After RNase treatment, the vast majority of Ku70/80 was derived from chromatin, but Y14 still remained (lane 3). A similar result was observed in MCF7 and HEK293 cells (Figure S7A). Therefore, RNA-independent chromatin association of Y14 suggested that it may directly interact with chromatin factor(s) of unknown identity (Figure S7B, upper). Nevertheless, we observed that IR or phleomycin treatment, which also causes DSBs, increased the level of Y14, Ku, and γH2AX on chromatin even after RNase treatment (Figures 4B for IR; S7C for phleomycin; Figure S7B, bottom). The ATM inhibitor KU55933 significantly reduced γH2AX signals on chromatin and slightly reduced the level of chromatin-bound Y14 (Figure 4C). Therefore, ATM-dependent Ku interaction and chromatin association of Y14 suggested its direct role in DNA repair.

Y14 Depletion Delays the Formation of DNA Damage Foci and Recruitment of DNA Repair Factors

Next, we evaluated the formation of DNA damage foci in Y14- or eIF4A3-depleted HeLa cells. Immunofluorescence using anti-Y14 or anti-eIF4A3 was able to distinguish transfected from non-transfected cells (Figure 5A; dashed circle for Y14- or eIF4A3-depleted cells and arrowhead for non-transfected cells). IR exposure induced γH2AX foci in non-transfected cells within 5 min (Figure 5A, arrowheads). γH2AX foci also formed in eIF4A3-depleted but not in Y14-depleted cells (Figure 5A, dashed circles, and Figure 5B, 3 min), suggesting that Y14 depletion specifically affects the formation of γH2AX foci. We performed a time course experiment and observed that the focus number was raised in Y14-depleted cells between

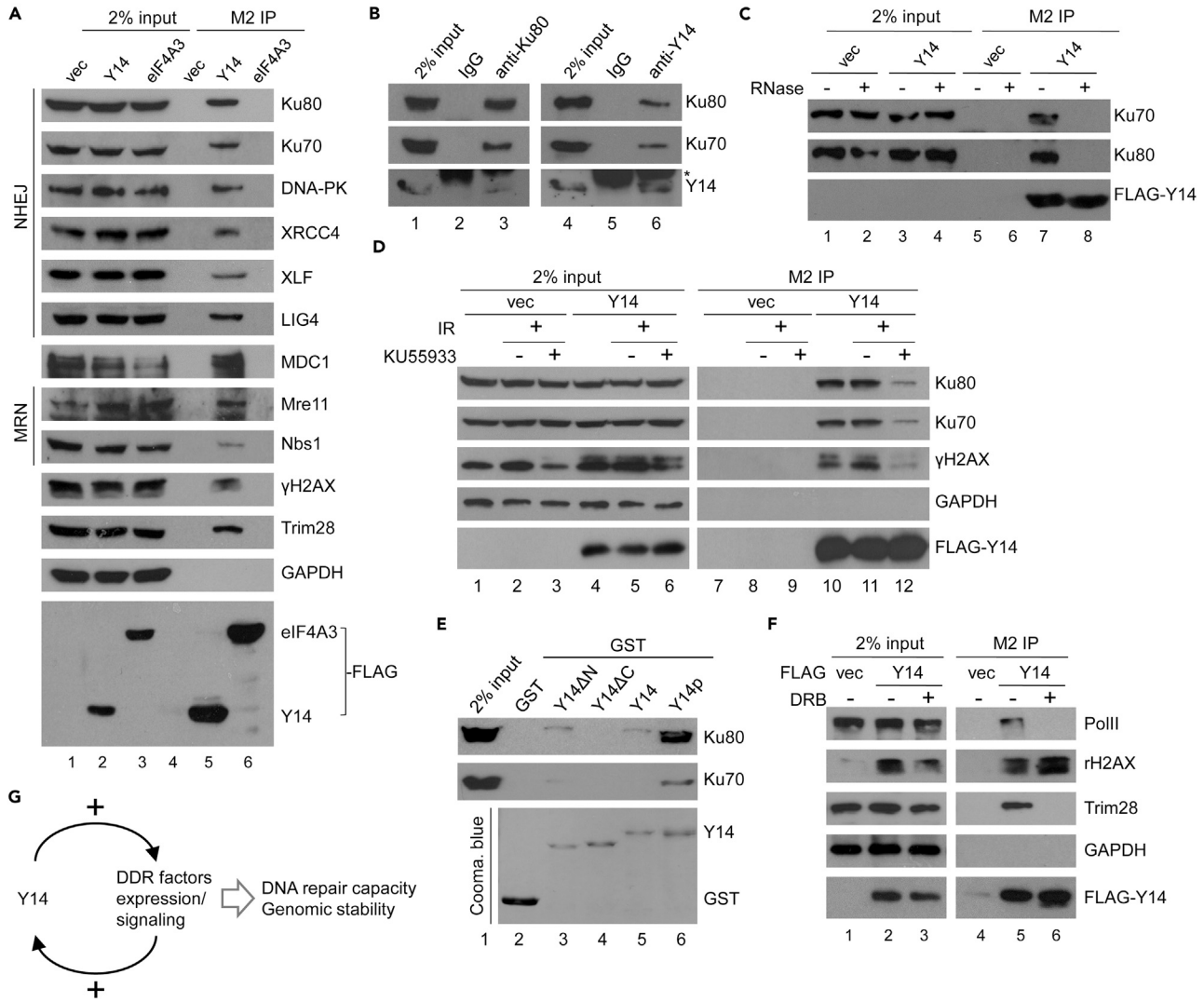

Figure 3. Y14 Interacts with DNA Damage Repair Factors

(A) HEK293 cells were transfected with empty vector (vec) or vector encoding FLAG-Y14 or FLAG-eIF4A3. Cell lysates were subjected to immunoprecipitation with anti-FLAG, followed by immunoblotting using antibodies against FLAG or indicated proteins.

(B) HEK293 cell lysates were subjected to immunoprecipitation using control IgG or anti-Ku or anti-Y14, followed by immunoblotting. Asterisk indicates the immunoglobulin light chain.

(C) HEK293 cells were transfected with the empty or FLAG-Y14 vector. Immunoprecipitation was performed using anti-FLAG in the cell lysates in the absence (–) or presence (+) of RNase A, followed by immunoblotting.

(D) Transfected cells as in (C) were left untreated or were treated with the ATM inhibitor KU55933, followed by 10 Gy irradiation. The cell lysates were each subjected to immunoprecipitation using anti-FLAG, followed by immunoblotting.

(E) *In vitro* pull-down assay was performed by incubating GST or GST-Y14 (full-length, ΔN, ΔC, or phosphorylated) with the HeLa cell lysate. Bound proteins were analyzed by immunoblotting using anti-Ku70/80. GST fusions were detected by Coomassie blue staining.

(F) HEK293 cells were transfected with the empty (vec) or FLAG-Y14 vector. FLAG-Y14 transfectants were mock treated or treated with the RNA polymerase II inhibitor DRB. Anti-FLAG immunoprecipitates were subjected to immunoblotting.

(G) Model shows the role of Y14 in a positive circuit of DDR signaling. Y14 promotes the expression of several DDR factors including ATM, which is likely required for Y14 function in DNA damage repair.

15 and 30 min after exposure (Figure 5B), indicating that Y14 depletion delayed, but did not completely block, γH2AX foci formation. This delay may have partially resulted from defective DDR signaling in Y14-deficient cells, although there still could be a direct role for Y14 in recruiting DNA repair factors to damaged sites.

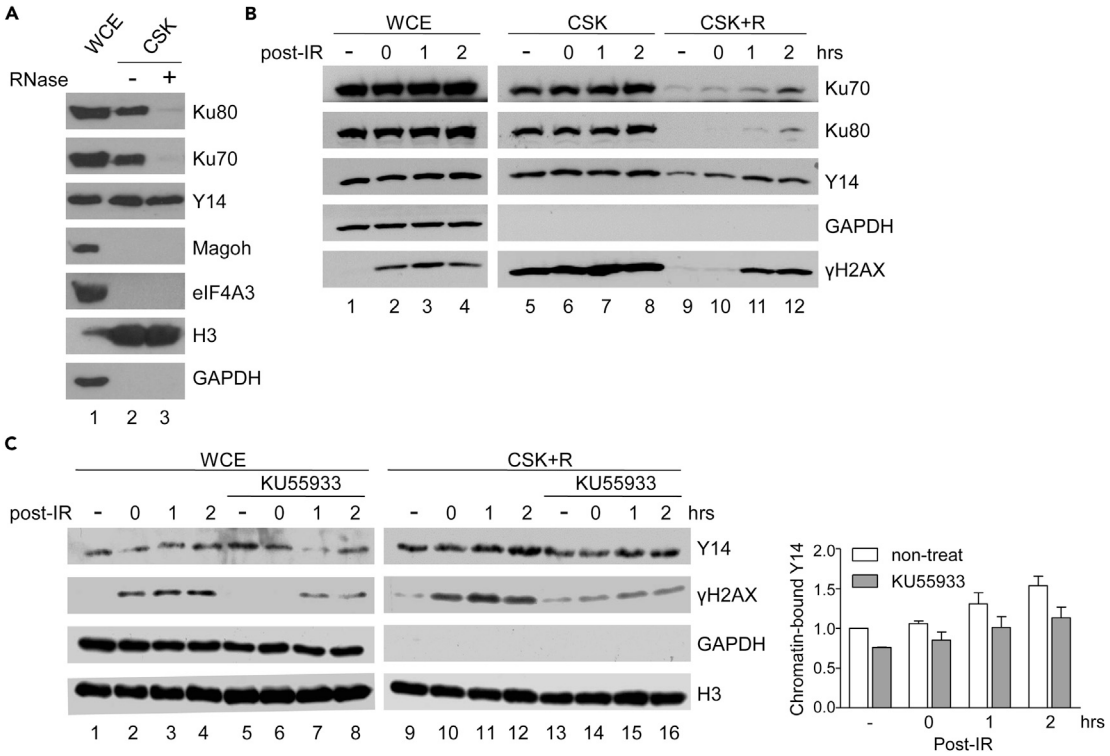

Figure 4. Y14 Associates with Chromatin and Accumulates on Chromatin after DNA Damage

(A) Immunoblotting was performed using the whole-cell extract (WCE) and RNase A-treated (+) and non-treated (–) chromatin fractions (CSK) of HeLa cells.

(B) HeLa cells were mock-irradiated (–) or irradiated with 10 Gy followed by recovery for 0, 1, or 2 h. Immunoblotting shows the indicated proteins in the WCE and RNase-treated (CSK + R) and non-treated (CSK) chromatin fractions.

(C) HeLa cells were mock-treated or treated with KU55933 followed by IR irradiation and subsequent recovery. The WCE and RNase-treated chromatin fraction (CSK + R) were subjected to immunoblotting. Bar graph shows the relative level of chromatin-bound Y14 without (lanes 9–12) or after KU55933 treatment (lanes 13–16); lane 9 was set as 1.

To more precisely assess the molecular mechanism by which Y14 modulates the formation of foci, we used live-cell imaging to track the dynamic mobilization of MDC1 and Ku70/80 after laser-induced DNA damage. MDC1 is a key mediator of the DDR that recognizes γH2AX (Chapman et al., 2012). GFP-tagged MDC1 steadily accumulated at sites of DNA damage, consistent with a previous report (Chang et al., 2015), and this accumulation significantly slowed upon transfection of a Y14 small hairpin RNA-expressing vector (Figure 5C). Analogously, the recruitment of GFP-tagged Ku70 and Ku80 was also delayed upon Y14 depletion (Figures 5D and 5E, lower panels), supporting the notion that Y14 is required for the early assembly of DSB repair complexes.

Y14 Depletion Disrupts the Ubiquitination of Ku and Impairs DNA Repair

Y14 accumulated on chromatin after DNA damage and may facilitate Ku recruitment to DNA lesions (Figures 4 and 5). Intriguingly, we observed that Y14 depletion, however, resulted in Ku accumulation on chromatin following phleomycin treatment (Figure 6A). Depletion of eIF4A3 had no such effect compared with control (Figure S8). It has been reported that ubiquitination modulates the release of Ku70/80 from DNA lesions after repair (Brown et al., 2015), so we examined whether Y14 may influence Ku ubiquitination. Ubiquitination of overexpressed FLAG-Ku70 was enhanced upon phleomycin treatment (Figure 6B, lane 3), as reported (Brown et al., 2015). Y14 depletion diminished Ku ubiquitination by ~60% (lane 4 and bar graph). This result suggested that Y14 may modulate the ubiquitination of Ku and provided an explanation for our observed persistence of Ku70/80 on chromatin in Y14-depleted cells.

Next, we tested whether Y14 depletion could affect DNA repair using a previously characterized NHEJ reporter, pEGFP-Pem1-Ad2 (Seluanov et al., 2004). The I-*Sce*I- or *Hind*III-digested reporter plasmid was transfected into U2OS cells, as per the instruction of Seluanov et al. (2004). Unlike complementary ends

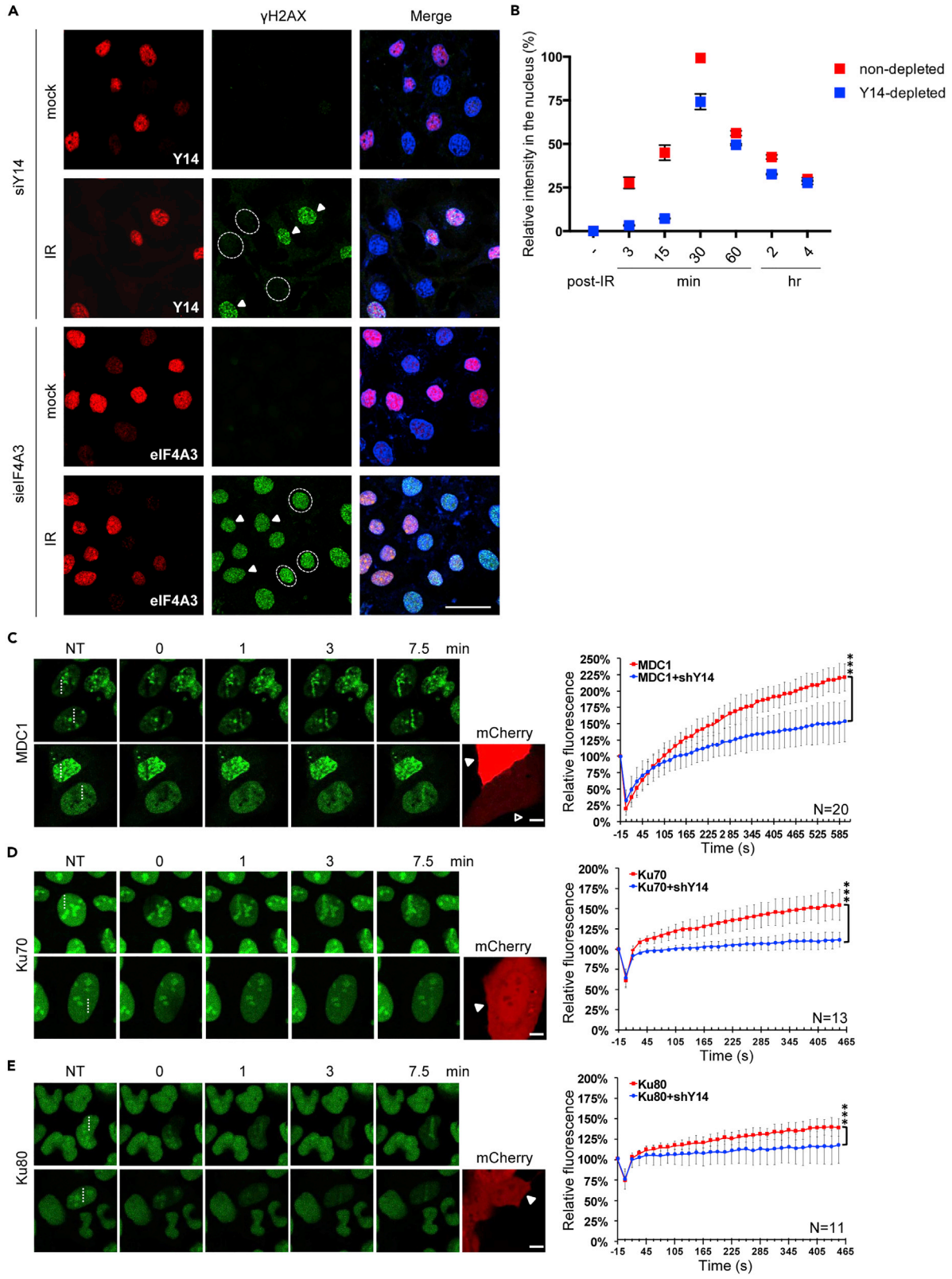
A
γH2AX
Merge
siY14
mock
IR
Y14
siIF4A3
eIF4A3
B
Relative intensity in the nucleus (%)
non-depleted
Y14-depleted
post-IR
min
hr
C
NT
0
1
3
7.5
min
MDC1
mCherry
MDC1
MDC1+shY14
Relative fluorescence
Time (s)
N=20
D
Ku70
Ku70+shY14
N=13
E
Ku80
Ku80+shY14
N=11

Figure 5. Y14 Depletion Delays the Formation of DNA Damage Foci and Recruitment of DNA Repair Factors

(A) HeLa cells were transfected with an siRNA targeting Y14 or eIF4A3 for 48 h and then left non-irradiated or irradiated at 10 Gy. Cells were fixed 3 min to 4 h (see B) after IR treatment, followed by immunofluorescence using antibodies against Y14, eIF4A3, and γH2AX and Hoechst staining. Representative images show 3-min post-IR. Dashed circle indicate Y14- or eIF4A3-depleted cells, and arrowheads indicate non-transfected cells; three selected cells are indicated. Scale bar, 20 μm.

(B) The experiment was as described in (A). The fluorescence intensities of γH2AX were scored using ImageJ from at least 30 cells per condition. Bar graph shows the relative γH2AX intensity (mean ± SD) of Y14-depleted cells versus non-depleted cells at the indicated time points.

(C–E) U2OS cells that stably expressed the GFP fusion with (C) MDC1, (D) Ku70, or (E) Ku80 were transiently transfected with the Y14 shRNA-mCherry-expressing vectors. Cells were subjected to laser microirradiation (405 nm) followed by live-cell imaging using confocal microscopy. Representative confocal images show accumulation of GFP fusion proteins at sites (dashed lines) of laser microirradiation at the indicated time points. NT indicates samples before microirradiation. The intensity (high, arrowhead; low, empty triangle) of mCherry represents the expression level of shY14. Curve graphs show fluorescence intensities of GFP-fusion proteins at the irradiated region that were quantified periodically, normalized, and presented as mean ± SD for at least 10 cells in each experiment. Scale bar, 10 μm.

that can be joined via simple ligation, end repair of DSB-mimicking I-*Sce*I-generated inverted overhangs involves nucleolytic end processing. Depletion of Y14 reduced the rejoining efficiency of the I-*Sce*I-linearized plasmid (Figure 6C). Overexpression of the siY14-resistent FLAG-Y14 (Y14R) in Y14-depleted cells restored end joining (Figure 6D), supporting a role for Y14 in DNA repair. Because inhibition of ATM reduced the phosphorylation of Y14 (Figure S6D), we tested the effect of a non-phosphorylatable Y14 mutant (SA) on DNA repair. We found that Y14-SA had a dominant-negative effect on DNA repair, even though it was expressed poorly (Figure 6E). As observed in U2OS cells, knockdown of Y14 or overexpression of Y14-SA also reduced the end joining efficiency in HeLa cells (Figures S9A and S9B), supporting the role of Y14 in DNA repair. Knockdown of eIF4A3, although had no significant effect in U2OS cells (Figure 6C), suppressed end joining to an extent equivalent to Y14 depletion in HeLa cells (Figure S9B); whether eIF4A3 modulates DSB repair via a mechanism different from that of Y14 remains to be investigated.

Finally, to examine whether Y14 indeed associates with DSBs, we took advantage of a line of U2OS cells that have a stably integrated GFP reporter with an I-*Sce*I recognition site (Gunn et al., 2011). Chromatin immunoprecipitation and qPCR revealed that FLAG-Y14 associated with the GFP reporter upon cleavage by transiently expressed I-*Sce*I; a similar result was obtained with FLAG-Ku70 (Figure 6F). The association of FLAG-Ku70 with the cleaved reporter was diminished by ~20% in Y14-depleted cells (Figure 6G), suggesting that Y14 facilitates or stabilizes Ku binding to DNA ends. Together, our results indicated two possible direct roles for Y14 in DNA repair, i.e., recruiting Ku to DNA lesions and modulating its ubiquitination, both of which influence DNA repair efficiency.

In conclusion, Y14 acts through multiple pathways to maintain genome stability. First, Y14 is essential for the expression of several DDR factors, which maintains cellular capacity for DNA damage repair, and also functions to prevent R-loop accumulation during transcription (Figure 7, left). Moreover, upon DNA damage, Y14 promotes the recruitment of DDR factors to DNA lesions and perhaps also orchestrates their functions in DNA repair (Figure 7). Depletion of Y14 reduces DNA repair efficiency. Hence Y14 deficiency results in DNA damage accumulation in cultured cells and in the developing neocortex.

DISCUSSION

We have previously reported that Y14 depletion resulted in the accumulation of a DNA damage marker and sensitized cells to irradiation (Lu et al., 2017). This study reveals that Y14 not only indirectly but also directly contributes to genome stability. We provide evidence for the functions of Y14 in DDR signaling and DSB repair.

Previous studies have reported that depletion of Y14 alters the splicing pattern of apoptotic and cell-cycle-related genes (Michelle et al., 2012; Wang et al., 2014; Fukumura et al., 2016; Lu et al., 2017), which likely threatens cell viability. Here, we show that depletion of Y14 downregulated several DDR factors, including three critical DDR kinases (Figure 2), leading to attenuated DDR signaling and inefficient DSB repair. Moreover, depletion of Y14 induced R-loops (Figure 2). Thus, as many other splicing factors and the THOC (Naro et al., 2015; Wickramasinghe and Venkitaraman, 2016), Y14 prevents co-transcriptional aberrant R-loop formation. It is not surprising to observe that depletion of eIF4A3 also compromised the expression of DDR factors and induced R-loops (Figures S4 and S5). Therefore, Y14, eIF4A3, and perhaps other EJC factors likely via their role in RNA processing maintain proper expression of DDR factors and prevent R-loop

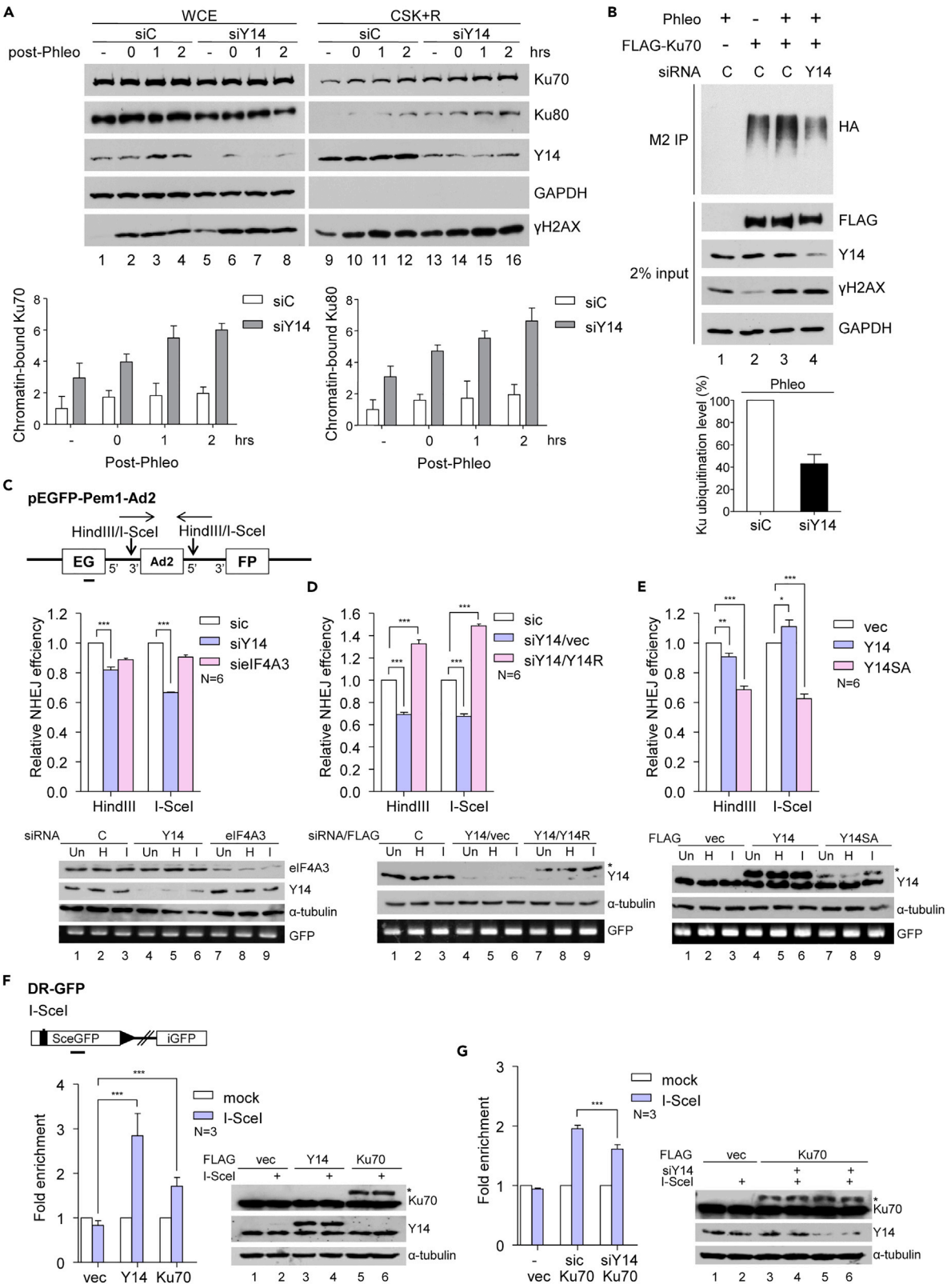
A
WCE
CSK+R
siC
siY14
post-Phleo
hrs
Ku70
Ku80
Y14
GAPDH
γH2AX
Chromatin-bound Ku70
Chromatin-bound Ku80
Post-Phleo
B
Phleo
FLAG-Ku70
siRNA
M2 IP
HA
2% input
FLAG
Ku ubiquitination level (%)
C
pEGFP-Pem1-Ad2
HindIII/I-SceI
EG
Ad2
FP
Relative NHEJ efficiency
sic
siY14
sieIF4A3
N=6
HindIII
I-SceI
siRNA
eIF4A3
α-tubulin
GFP
D
siY14/vec
siY14/Y14R
siRNA/FLAG
E
vec
Y14
Y14SA
F
DR-GFP
SceGFP
iGFP
Fold enrichment
mock
N=3
Ku70
G

Figure 6. Y14 Depletion Disrupts Ku Ubiquitination and Impairs DNA Repair

(A) siC or siY14-transfected HeLa cells were mock treated (−) or treated with phleomycin, followed by recovery for 0, 1, or 2 h. WCE and CSK + R (see Figure 4B) were subjected to immunoblotting. Bar graph shows the relative level of chromatin-bound Ku70/80 in siC (lanes 9–12) and siY14 cells (lanes 13–16); lane 9 was set as 1.

(B) HEK293 cells were transfected with vectors or siRNA (HA-ubiquitin, lanes 1–4; FLAG-Ku70, lanes 2–4; siC, lanes 1–3; siY14, lane 4), and then mock treated (lane 2) or treated with phleomycin (lanes 1, 3, 4). Immunoprecipitation was performed using anti-FLAG, followed by immunoblotting. Bar graph shows the level of Ku ubiquitination in Y14-depleted cells (lane 5) versus control cells (lane 4) after phleomycin treatment.

(C) Diagram shows the pEGFP-Pem1-Ad2 vector as the NHEJ reporter (Seluanov et al., 2004). U2OS cells were co-transfected with uncut (Un), *Hind*III (H)-, or I-*Sce*I (I)-digested NHEJ reporter and siRNA as indicated. The number of GFP-expressing cells was determined by fluorescence-activated cell sorting and normalized by the transfection rate (i.e., the level of GFP PCR product). (C–E) Bar graphs show end joining efficiency (mean ± SD) relative to siC. Immunoblotting shows knockdown or overexpressed proteins; PCR of a GFP fragment (horizontal line in the diagram; primers in Table S2) was used as the transfection control.

(D) U2OS cells were transfected with the reporter as in (C), siRNA (siC or siY14), and expression vector (empty or FLAG-Y14R encoding siRNA-resistant Y14). Asterisk indicates FLAG-tagged proteins (D–G).

(E) U2OS cells were transfected with the reporter as in (C) and expression vector (empty or FLAG-Y14 or FLAG-Y14SA).

(F) Diagram shows the DR-GFP construct that is genomically integrated in U2OS cells (U2OS-HDR; Gunn et al., 2011). U2OS-HDR cells were co-transfected with the empty or vector encoding FLAG-Y14 or FLAG-Ku70 and the I-*Sce*I (white bar) expression vector. (F and G) Bar graphs show relative fold-enrichment of precipitated DNA determined by qPCR; mock transfection was set as 1. Immunoblotting shows knockdown or overexpressed proteins as in (C–E).

(G) U2OS-HDR cells were co-transfected with siRNA (mock, siC or siY14) and the empty or FLAG-Ku70 expression vector and the I-*Sce*I vector.

accumulation, and thereby contribute to genome stability. Nevertheless, in this regard, whether they act independently or in the EJC context is not addressed in this study.

We observed that Y14 depletion delayed DDR kinetics, i.e., recruitment of DDR factors and formation of γH2AX foci (Figure 5). Although this may in part result from downregulated DDR signaling, our results argue for a direct role for Y14 in DNA signaling and repair. Most importantly, Y14 interacted with DNA damage-sensing, signaling, and repair factors in an EJC-independent manner (Figure 3) and was detected in EJC-deficient chromatin (Figure 4). Moreover, Y14 may possibly associate with some unknown chromatin factor(s) in an RNA-independent manner. DNA damage further enhanced the localization of Y14 to chromatin (Figure 4). However, we were unable to detect Y14 in laser-induced DNA damage sites by live cell imaging (data not shown), perhaps due to its transient or loose association with DNA damage sites. Our observation is in line with previous reports for several RNA processing factors that exhibit dynamic localization at sites of DNA damage (reviewed in Wickramasinghe and Venkitaraman, 2016). Moreover, we found that Y14 depletion diminished ubiquitination of Ku and may hence increase its retention on chromatin (Figure 6). This result is reminiscent of our previous report that Y14 modulates p53 ubiquitination (Lu et al., 2017), but the underlying molecular mechanism remains elusive at present. A recent report indicates that the paraspeckle factor RBM14 also regulates Ku retention during NHEJ-mediated DNA repair (Simon et al., 2017). Therefore a set of RNA-binding proteins may modulate Ku dynamics on chromatin during DNA damage repair. RNA-dependent interaction between Y14 and Ku is not completely unexpected, because non-coding RNAs as well as small RNAs generated at DNA damage loci have been implicated in DDR signaling and DNA repair (d'Adda di Fagagna, 2014). Therefore, whether Y14-mediated Ku recruitment involves RNA and whether Y14 participates in DNA damage-induced RNA processing at damage sites are intriguing topics for future study.

Our results indicate that DDR signaling may modulate Y14 function in DNA repair. Inactivation of ATM reduced the phosphorylation level of Y14 and abolished its interaction with Ku and accumulation on chromatin (Figures 3, 4, and S6). Overexpression of a non-phosphorylatable mutant of Y14 caused a dominant-negative effect on DNA end joining. These results suggest that phosphorylation of Y14 by ATM or as-yet-unidentified kinases is important for DNA repair. It is also notable that Y14 maintains the expression of ATM and several other DDR signaling factors (Figure 2). Therefore, Y14 is possibly engaged in a positive circuit to maintain DNA repair capacity (Figure 3), which emphasizes the importance of Y14 in genome integrity.

In this study, we found a transcription-dependent Y14-Trim28 interaction (Figure 3). Trim28 stabilizes RNA polymerase II pausing at the promoter-proximal region. Upon transcriptional activation, DDR factors associated with topoisomerase II-induced DSBs at promoters phosphorylate Trim28, leading to its release and subsequent transcriptional elongation (Bunch et al., 2015). We indeed observed that Y14 is possibly involved in stimulus-induced transcription through its interaction with Trim28 (data not shown). Notably, a recent report indicates that the nuclear EJC is required for Pol II pausing that prevents premature

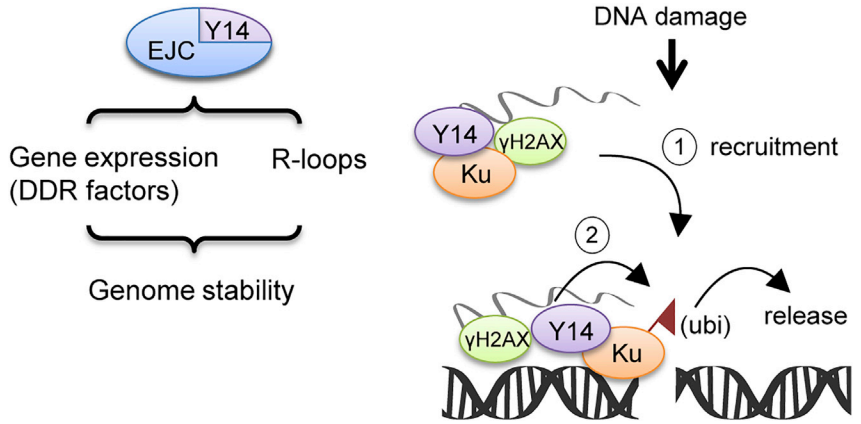

Figure 7. Model of both Direct and Indirect Roles of Y14 in Genome Stability

Y14 maintains proper expression of DDR factors and prevents the formation of co-transcriptional R-loops likely through its role as an EJC factor (left). Y14 may directly participate in DNA damage repair via its RNA-mediated interaction with Ku and other DDR factors. Upon DNA damage, Y14 promotes Ku and DDR factors to DNA lesion and modulates Ku ubiquitination (ubi) and release after repair (right). Y14 deficiency impairs NHEJ.

transcriptional elongation (Akhtar et al., 2018). Therefore whether the individual components of the EJC have any specific role in stimulus-induced pause release remains a topic of future investigation.

In conclusion, Y14 plays a direct role in DNA damage repair via its unprecedented interaction with DNA repair factors and also maintains DDR signaling and prevents co-transcriptional R-loops. Y14 deficiency hampers early brain development at least in part from accumulated DNA damage and genome instability.

Limitations of the Study

This study provides initial evidence for the direct role of Y14 in DNA damage repair. The detailed mechanism by which how Y14 modulates Ku association with DNA damage sites and the possibility of whether any specific RNA molecules are involved in Y14-mediated Ku recruitment during DNA damage repair remain to be investigated.

METHODS

All methods can be found in the accompanying Transparent Methods supplemental file.

SUPPLEMENTAL INFORMATION

Supplemental Information can be found online at https://doi.org/10.1016/j.isci.2019.03.005.

ACKNOWLEDGMENTS

We thank J. M. Stark, V. Gorbunova, K. R. Jones, and A. Aguilera for the plasmids, cell lines, mouse lines, antibodies, and experimental suggestions. We also thank the Proteomics and Animal Cores of the Institute of Biomedical Sciences, the Transgenic Facility of the Institute of Molecular Biology, the Imaging and Cell Biology Facility of the Institute of Biological Chemistry for technique assistance, and Timothy C. Taylor for proofreading of the manuscript. We acknowledge Taiwan Protein Project of Academia Sinica grant AS-KPQ-105-TPP to P.-Y.W. This work was primarily supported by the Ministry of Science and Technology grant 106-2311-B-001-019 to W.-Y.T.

AUTHOR CONTRIBUTIONS

W.-Y.T. oversaw all aspects of the project and wrote the manuscript. Figures were provided by T.-W.C. (Figures 1B, 3A–3F, 4A, 5A, 5B, S1, S3B, S6A–S6C, S7A, and S8), C.-C. Lu (Figures 1A, 2C, 4C, 6C–6G, S1, S3A, S3C, S4, S6D, S7C, S9A, and S9B), C.-H.S. (Figures 1D–1F, S2F, and S2G), P.-Y.W. (Figures 5C–5E), S.E. (Figures 2E, and S5A–S5F), C.-C. Lee (Figures 1C, 2A, 2B, 2D, and S2E), H.-C.K. (Figures 4B, 6A, and 6B), and K.-Y.H. (Figures S2B–S2D). Also, T.-W.C. contributed to the analysis of mass spectrometry

data and manuscript preparation, P.-Y.W. provided experimental and manuscript suggestions, K.-Y.H. contributed to mouse breeding and maintenance, K.-M.L. performed immunoprecipitation and mass spectrometry, and C.-Y.T. designed and generated the *Rbm8a-loxp* mice.

DECLARATION OF INTERESTS

The authors declare no conflicts of interest.

Received: August 19, 2018
Revised: January 8, 2019
Accepted: March 4, 2019
Published: March 29, 2019

REFERENCES

Akhtar, J., Kreim, N., Marini, F., Mohana, G.K., Brune, D., Binder, H., and Roignant, J.-Y. (2018). The exon junction complex regulates the release and phosphorylation of paused RNA polymerase II. BioRxiv, preprint.

Bhatia, V., Barroso, S.I., Garcia-Rubio, M.L., Tumini, E., Herrera-Moyano, E., and Aguilera, A. (2014). BRCA2 prevents R-loop accumulation and associates with TREX-2 mRNA export factor PCID2. Nature *511*, 362–365.

Brown, J.S., Lukashchuk, N., Sczaniecka-Clift, M., Britton, S., le Sage, C., Calsou, P., Beli, P., Galanty, Y., and Jackson, S.P. (2015). Neddylation promotes ubiquitylation and release of Ku from DNA-damage sites. Cell Rep. *11*, 704–714.

Bunch, H., and Calderwood, S.K. (2015). TRIM28 as a novel transcriptional elongation factor. BMC Mol. Biol. *16*, 14.

Bunch, H., Lawney, B.P., Lin, Y.F., Asaithamby, A., Murshid, A., Wang, Y.E., Chen, B.P., and Calderwood, S.K. (2015). Transcriptional elongation requires DNA break-induced signalling. Nat. Commun. *6*, 10191.

Chang, C.F., Chu, P.C., Wu, P.Y., Yu, M.Y., Lee, J.Y., Tsai, M.D., and Chang, M.S. (2015). PHRF1 promotes genome integrity by modulating non-homologous end-joining. Cell Death Dis. *6*, e1716.

Chapman, J.R., Taylor, M.R., and Boulton, S.J. (2012). Playing the end game: DNA double-strand break repair pathway choice. Mol. Cell *47*, 497–510.

Chuang, T.W., Lee, K.M., and Tarn, W.Y. (2015). Function and pathological implications of exon junction complex factor Y14. Biomolecules *5*, 343–355.

d'Adda di Fagagna, F. (2014). A direct role for small non-coding RNAs in DNA damage response. Trends Cell Biol. *24*, 171–178.

Fukumura, K., Wakabayashi, S., Kataoka, N., Sakamoto, H., Suzuki, Y., Nakai, K., Mayeda, A., and Inoue, K. (2016). The exon junction complex controls the efficient and faithful splicing of a subset of transcripts involved in mitotic cell-cycle progression. Int. J. Mol. Sci. *17*, 1153.

Gorski, J.A., Talley, T., Qiu, M., Puelles, L., Rubenstein, J.L., and Jones, K.R. (2002). Cortical excitatory neurons and glia, but not GABAergic neurons, are produced in the Emx1-expressing lineage. J. Neurosci. *22*, 6309–6314.

Gunn, A., Bennardo, N., Cheng, A., and Stark, J.M. (2011). Correct end use during end joining of multiple chromosomal double strand breaks is influenced by repair protein RAD50, DNA-dependent protein kinase DNA-PKcs, and transcription context. J. Biol. Chem. *286*, 42470–42482.

Hawley, B.R., Lu, W.T., Wilczynska, A., and Bushell, M. (2017). The emerging role of RNAs in DNA damage repair. Cell Death Differ. *24*, 1989.

Hsu Ia, W., Hsu, M., Li, C., Chuang, T.W., Lin, R.I., and Tarn, W.Y. (2005). Phosphorylation of Y14 modulates its interaction with proteins involved in mRNA metabolism and influences its methylation. J. Biol. Chem. *280*, 34507–34512.

Ishigaki, Y., Nakamura, Y., Tatsuno, T., Hashimoto, M., Shimasaki, T., Iwabuchi, K., and Tomosugi, N. (2013). Depletion of RNA-binding protein RBM8A (Y14) causes cell cycle deficiency and apoptosis in human cells. Exp. Biol. Med. (Maywood) *238*, 889–897.

Jackson, S.P., and Bartek, J. (2009). The DNA-damage response in human biology and disease. Nature *461*, 1071–1078.

Lu, C.C., Lee, C.C., Tseng, C.T., and Tarn, W.Y. (2017). Y14 governs p53 expression and modulates DNA damage sensitivity. Sci. Rep. *7*, 45558.

Mao, H., McMahon, J.J., Tsai, Y.H., Wang, Z., and Silver, D.L. (2016). Haploinsufficiency for core exon junction complex components disrupts embryonic neurogenesis and causes p53-mediated microcephaly. PLoS Genet. *12*, e1006282.

Mao, H., Pilaz, L.J., McMahon, J.J., Golzio, C., Wu, D., Shi, L., Katsanis, N., and Silver, D.L. (2015). Rbm8a haploinsufficiency disrupts embryonic cortical development resulting in microcephaly. J. Neurosci. *35*, 7003–7018.

Michelle, L., Cloutier, A., Toutant, J., Shkreta, L., Thibault, P., Durand, M., Garneau, D., Gendron, D., Lapointe, E., Couture, S., et al. (2012). Proteins associated with the exon junction complex also control the alternative splicing of apoptotic regulators. Mol. Cell. Biol. *32*, 954–967.

Naro, C., Bielli, P., Pagliarini, V., and Sette, C. (2015). The interplay between DNA damage response and RNA processing: the unexpected role of splicing factors as gatekeepers of genome stability. Front. Genet. *6*, 142.

Santos-Pereira, J.M., and Aguilera, A. (2015). R loops: new modulators of genome dynamics and function. Nat. Rev. Genet. *16*, 583–597.

Seluanov, A., Mittelman, D., Pereira-Smith, O.M., Wilson, J.H., and Gorbunova, V. (2004). DNA end joining becomes less efficient and more error-prone during cellular senescence. Proc. Natl. Acad. Sci. U S A *101*, 7624–7629.

Shkreta, L., and Chabot, B. (2015). The RNA splicing response to DNA damage. Biomolecules *5*, 2935–2977.

Simon, N.E., Yuan, M., and Kai, M. (2017). RNA-binding protein RBM14 regulates dissociation and association of non-homologous end joining proteins. Cell Cycle *16*, 1175–1180.

Sridhara, S.C., Carvalho, S., Grosso, A.R., Gallego-Paez, L.M., Carmo-Fonseca, M., and de Almeida, S.F. (2017). Transcription dynamics prevent RNA-mediated genomic instability through SRPK2-dependent DDX23 phosphorylation. Cell Rep. *18*, 334–343.

Wang, Z., Murigneux, V., and Le Hir, H. (2014). Transcriptome-wide modulation of splicing by the exon junction complex. Genome Biol. *15*, 551.

Wickramasinghe, V.O., and Venkitaraman, A.R. (2016). RNA processing and genome stability: cause and consequence. Mol. Cell *61*, 496–505.

ISCI, Volume *13*

Supplemental Information

The RNA Processing Factor Y14 Participates in DNA Damage Response and Repair

Tzu-Wei Chuang, Chia-Chen Lu, Chun-Hao Su, Pei-Yu Wu, Sarasvathi Easwvaran, Chi-Chieh Lee, Hung-Che Kuo, Kuan-Yang Hung, Kuo-Ming Lee, Ching-Yen Tsai, and Woan-Yuh Tarn

Supplemental Information (SI)

Supplemental Tables

Table S1: Mass-spectrometric Analysis of Y14-interacting Proteins. (Related to Table 1).

FLAG-Y14 was immunoprecipitated from HEK293 cells using anti-FLAG; co-immunoprecipitates identified by mass spectrometric analysis are functionally categorized.

Table S2: Primers Used in This Study. (Related to Figures 6 and S5).

Experiments/ Gene names	Sequences (5' to 3')
DRIP	
Egr1-F	TTCGGATTCCCGCAGTGT
Egr1-R	TCACTTTCCCCCCTTTATCCA
Apoe-F	CCGGTGAGAAGCGCAGTCGG
Apoe-R	CCCAAGCCCGACCCCGAGTA
Rpl13A-F	GCTTCCAGCACAGGACAGGTAT
Rpl13A-R	CACCCACTACCCGAGTTCAAG
Btbd19-F	CCCCAAAGGGTGGTGACTT
Btbd19-R	TTCACATTACCCAGACCAGACTGT
Intergenic-F	CTGTACCTGGGGTTCATTCATT
Intergenic-R	CAGTAAGCCGTTCACTCTCAC
End-joining assay	
GFP-F	GCTGGACGGCGACGTAAAC
GFP-R	GGTCTTGTAGTTGCCGTC
ChIP	
DR-GFP-F	CATGCCCGAAGGCTACGT
DR-GFP-R	CGGCGCGGGTCTTGTA

F, forward; R, reverse; TSS, transcription start site; GB, gene body

Figure S1

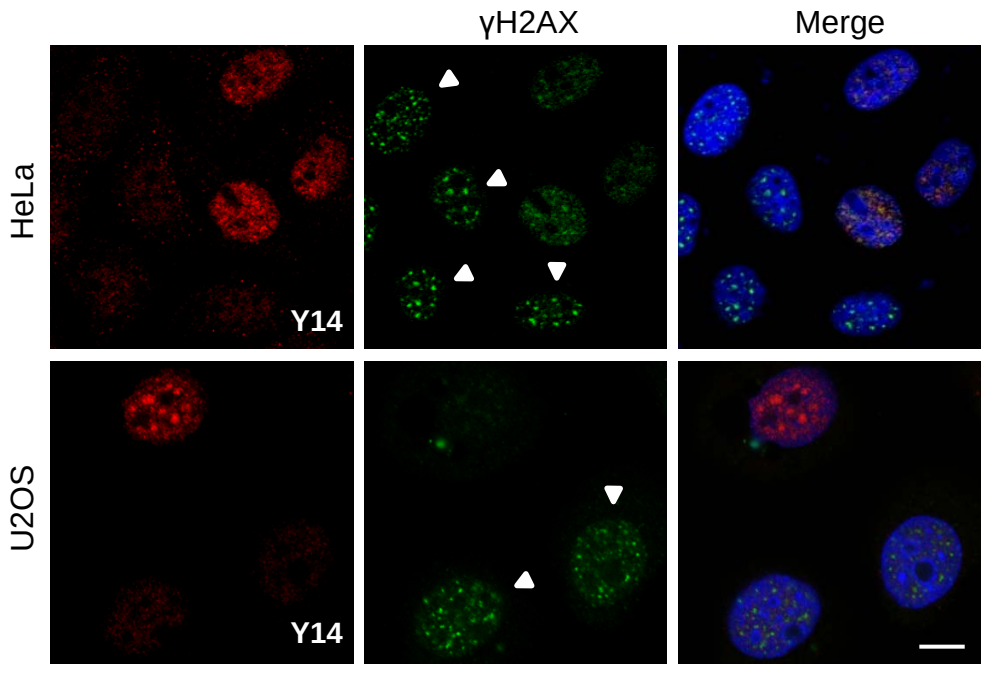

Figure S2

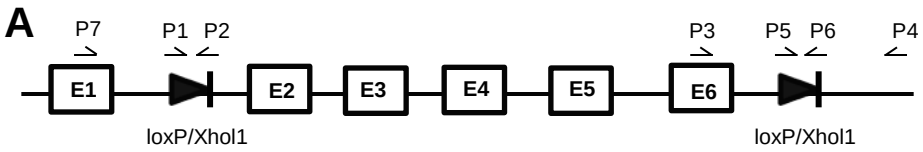
A
P7
P1 P2
P3
P5 P6
P4
E1
E2
E3
E4
E5
E6
loxP/Xhol1
loxP/Xhol1

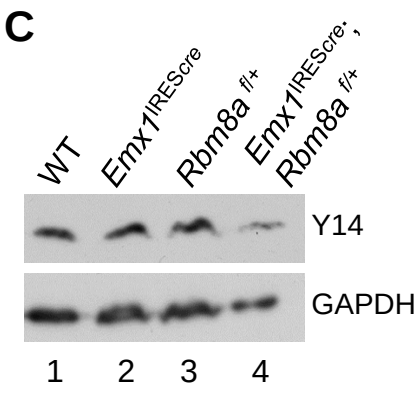
C
WT
Emx1IREScre
Rbm8a f/+
Emx1IREScre; Rbm8a f/+
Y14
GAPDH
1 2 3 4

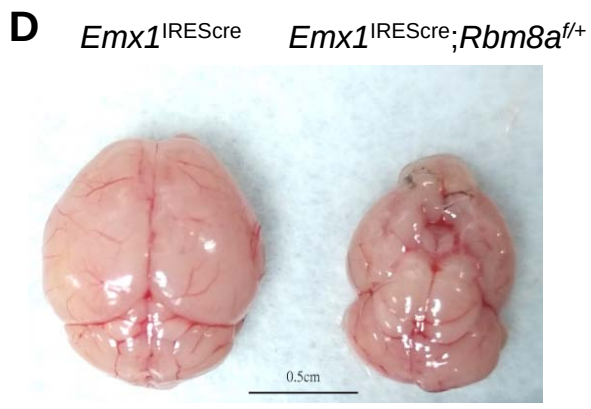
D
Emx1IREScre
Emx1IREScre;Rbm8af/+
0.5cm

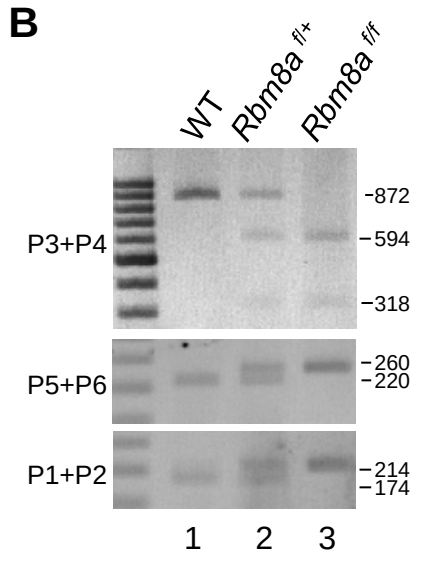
B
WT
Rbm8a f/+
Rbm8a f/f
P3+P4
P5+P6
P1+P2
872
594
318
260
220
214
174
1 2 3

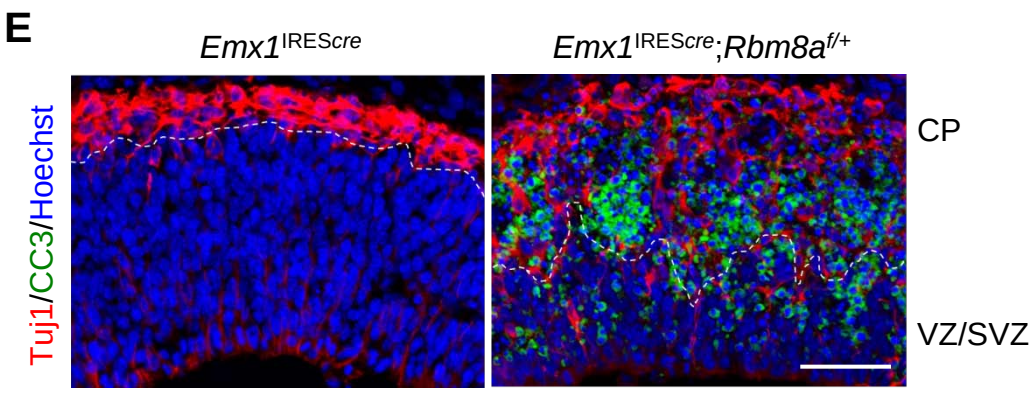
E
Emx1IREScre
Emx1IREScre;Rbm8af/+
Tuj1/CC3/Hoechst
CP
VZ/SVZ

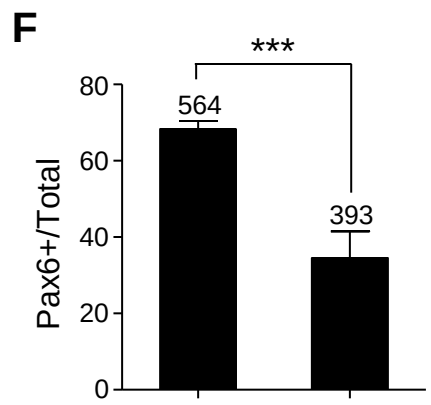
F
***
564
393
Pax6+/Total
80
60
40
20
0

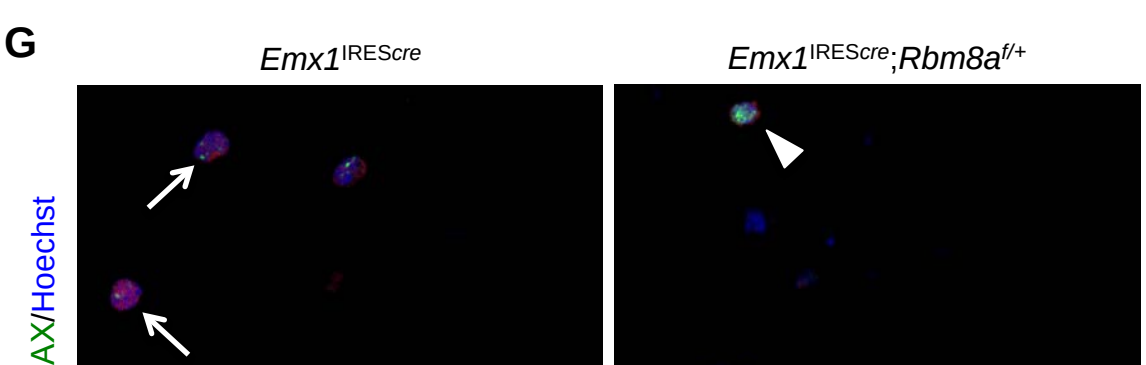
G
Emx1IREScre
Emx1IREScre;Rbm8af/+
Pax6/γH2AX/Hoechst
Pax6/CC3/Hoechst

Figure S3

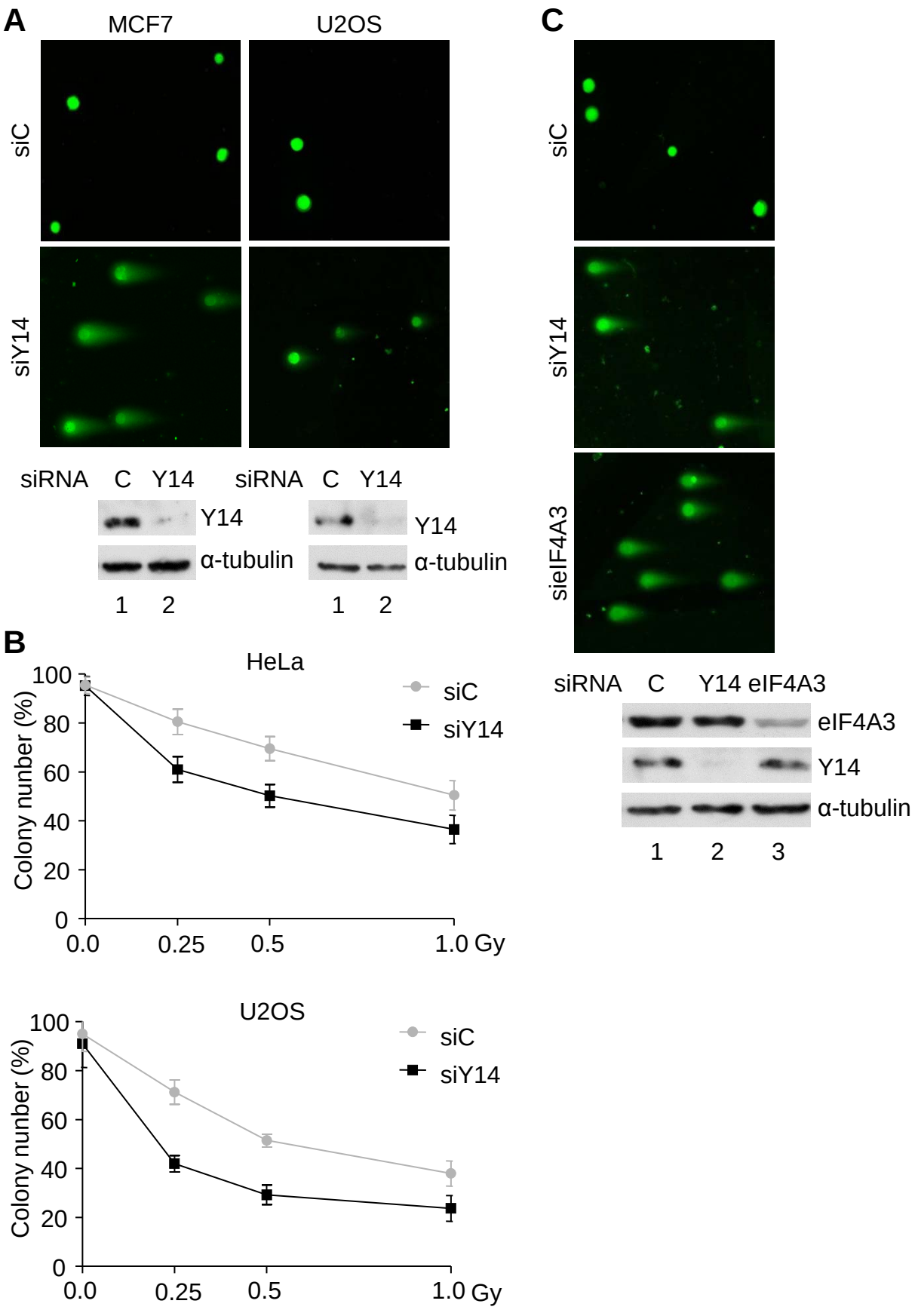
A
MCF7
U2OS
siC
siY14
siRNA C Y14
Y14
α-tubulin
1 2
B
HeLa
siC
siY14
Colony nunber (%)
100
80
60
40
20
0
0.0
0.25
0.5
1.0 Gy
U2OS
C
siC
siY14
sieIF4A3
siRNA C Y14 eIF4A3
eIF4A3
Y14
α-tubulin
1 2 3

Figure S4

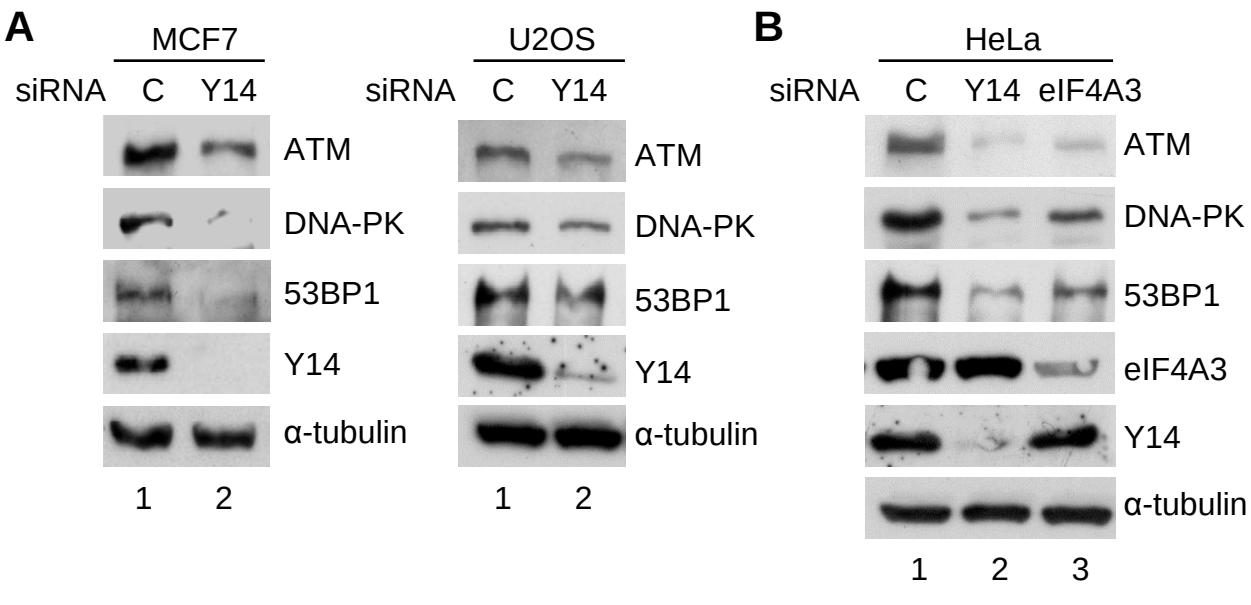
A
MCF7
siRNA C Y14
ATM
DNA-PK
53BP1
Y14
α-tubulin
1 2
U2OS
siRNA C Y14
ATM
DNA-PK
53BP1
Y14
α-tubulin
1 2
B
HeLa
siRNA C Y14 eIF4A3
ATM
DNA-PK
53BP1
eIF4A3
Y14
α-tubulin
1 2 3

Figure S5

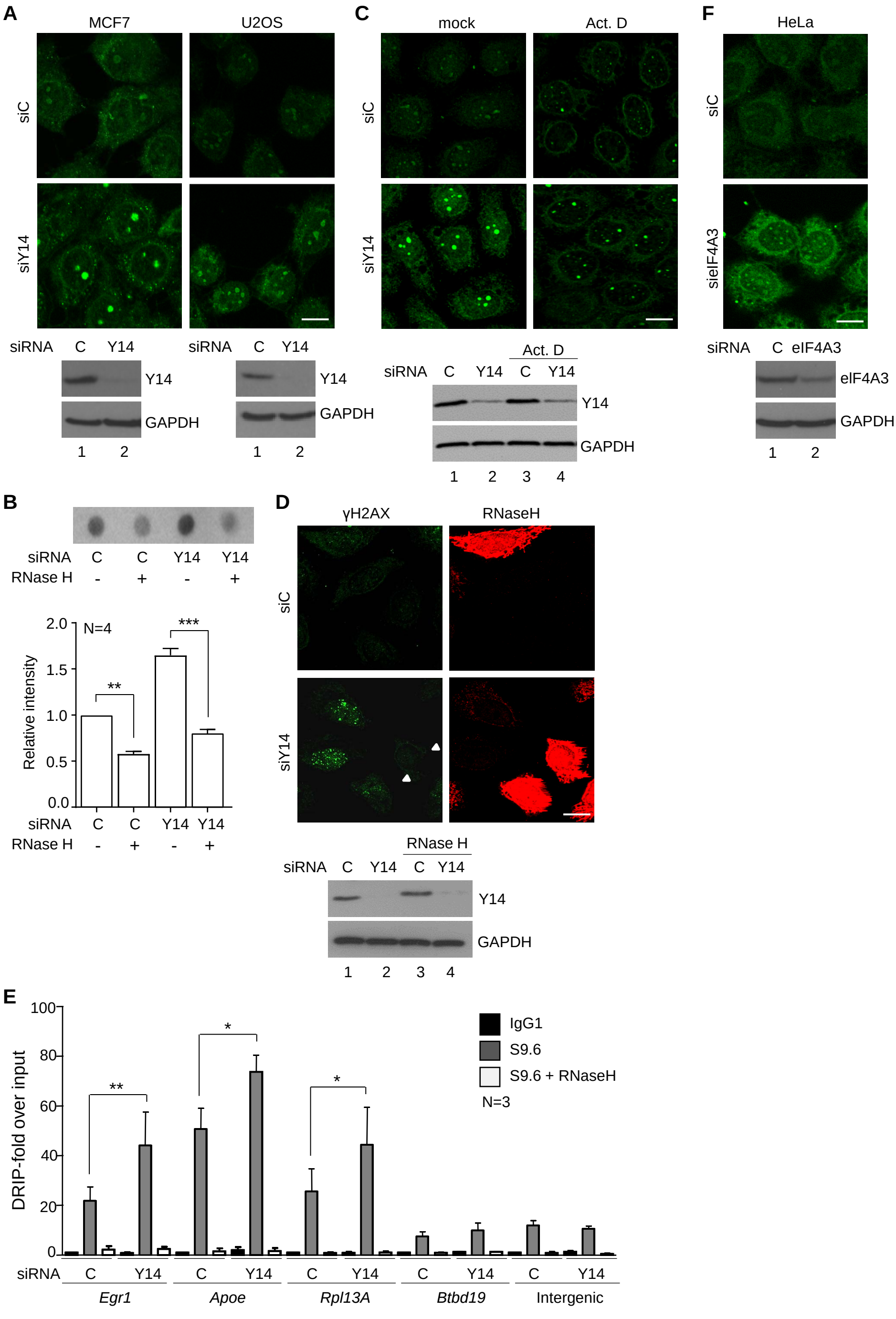
A
MCF7
U2OS
siC
siY14
siRNA C Y14
Y14
GAPDH
1 2
C
mock
Act. D
Act. D
siRNA C Y14 C Y14
F
HeLa
sieIF4A3
siRNA C eIF4A3
eIF4A3
B
siRNA C C Y14 Y14
RNase H - + - +
N=4
Relative intensity
2.0
1.5
1.0
0.5
0.0
**
***
D
γH2AX
RNaseH
1 2 3 4
RNase H
E
DRIP-fold over input
100
80
60
40
20
0
*
IgG1
S9.6
S9.6 + RNaseH
N=3
Egr1
Apoe
Rpl13A
Btbd19
Intergenic

Figure S6

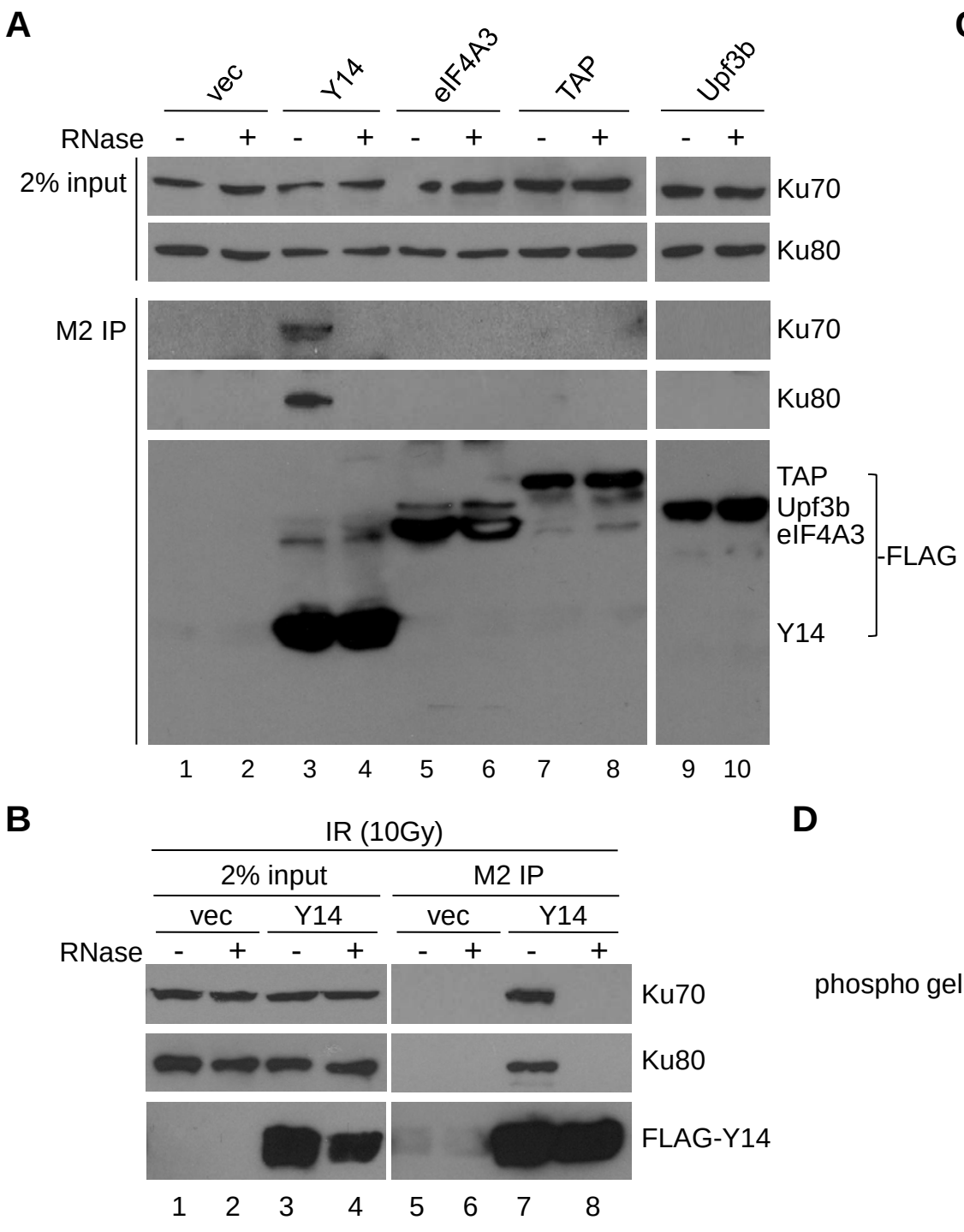
A
vec
Y14
eIF4A3
TAP
Upf3b
RNase
- + - + - + - + - +
2% input
Ku70
Ku80
M2 IP
Ku70
Ku80
TAP
Upf3b
eIF4A3
Y14
FLAG
1 2 3 4 5 6 7 8 9 10
B
IR (10Gy)
2% input
M2 IP
vec
Y14
vec
Y14
RNase
- + - + - + - +
Ku70
Ku80
FLAG-Y14
1 2 3 4 5 6 7 8
C
2% input
M2 IP
siATM
- + - +
vec
Y14
vec
Y14
vec
Y14
vec
Y14
ATM
Ku70
Ku80
Trim28
γH2AX
H2AX
FLAG-Y14
1 2 3 4 5 6 7 8
D
vec
FLAG-Y14
-
Caffeine
KU55933
-
Caffeine
KU55933
phospho gel
**
**
*
1 2 3 4 5 6

Figure S7

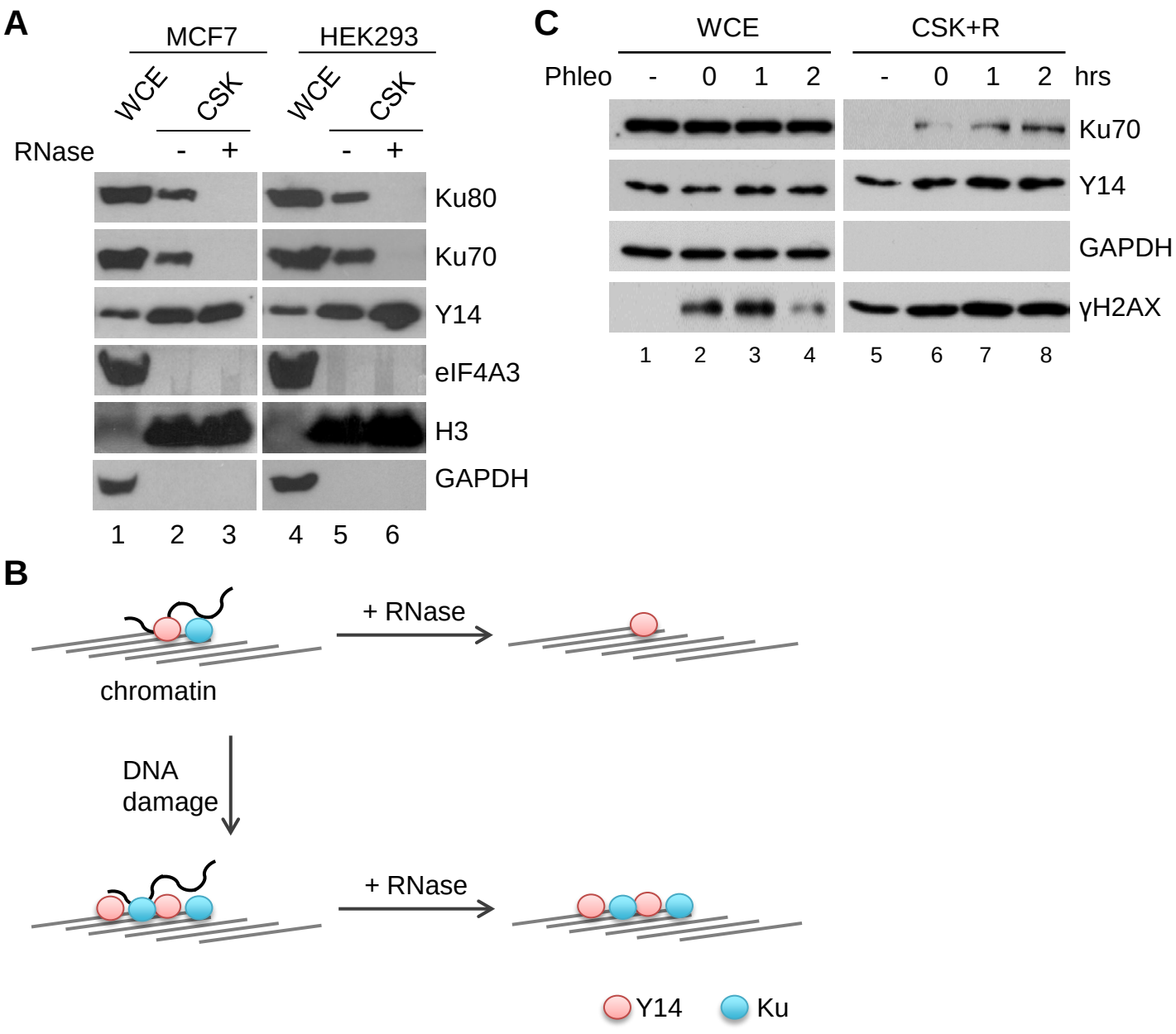
A
MCF7
HEK293
WCE
CSK
WCE
CSK
RNase
- + - +
Ku80
Ku70
Y14
eIF4A3
H3
GAPDH
1 2 3 4 5 6
C
WCE
CSK+R
Phleo - 0 1 2 - 0 1 2 hrs
Ku70
Y14
GAPDH
γH2AX
1 2 3 4 5 6 7 8
B
+ RNase
chromatin
DNA
damage
+ RNase
Y14
Ku

Figure S8

WCE
CSK+R
siC
sieIF4A3
Post-Phleo
- 0 2 - 0 2
- 0 2 - 0 2
Ku70
Ku80
eIF4A3
GAPDH
H3
1 2 3 4 5 6 7 8 9 10 11 12
Chromatin-bound Ku70
Chromatin-bound Ku80
2.0
1.5
1.0
0.5
0.0
siC
sieIF4A3
- 0 2 hrs
Post-Phleo

Figure S9

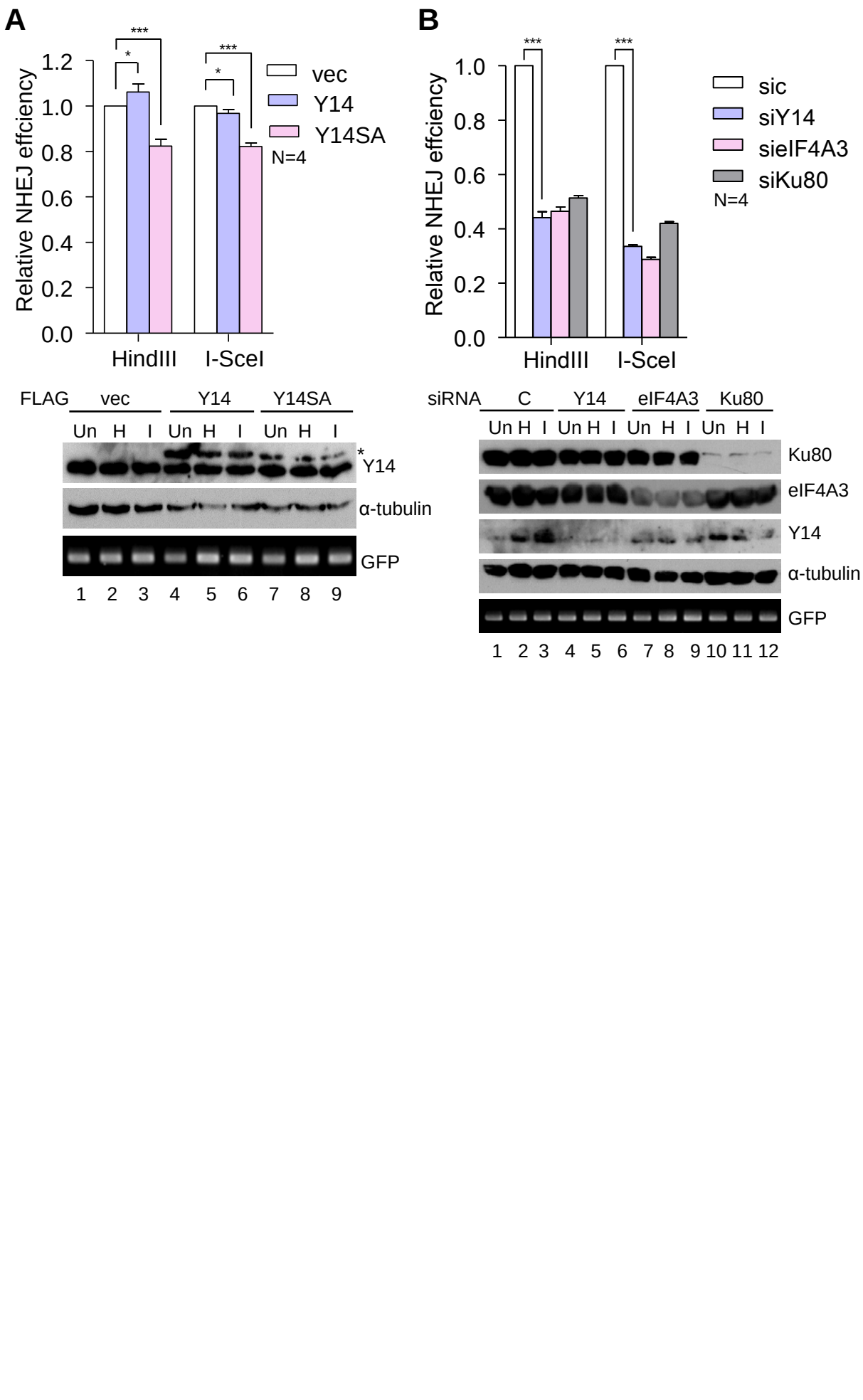
A
B
Relative NHEJ effciency
vec
Y14
Y14SA
N=4
HindIII
I-SceI
sic
siY14
sieIF4A3
siKu80
FLAG
siRNA
C
eIF4A3
Ku80
Un H I
Y14
α-tubulin
GFP
1 2 3 4 5 6 7 8 9
1 2 3 4 5 6 7 8 9 10 11 12

Supplemental Figure Legends

Figure S1. Y14 Depletion Induced γH2AX Foci. (Related to Figure 1).

HeLa and U2OS cells were transfected with siC or siY14 and subjected to immunostaining using anti-γH2AX and anti-Y14 and Hoechst staining. Arrowhead indicates Y14-depleted cells. Scale bar, 10 μm.

Figure S2. Generation and Characterization of the *Emx1*^{IREScre}*;Rbm8a*$^{f/+}$ Embryonic Brain. (Related to Figure 1).

(A) Schematic diagram shows the engineered mouse *Rbm8a* gene, in which the two loxp sites (arrowheads) were inserted into intron 1 and the 3' end, respectively. Primers used for genotyping are depicted; their sequences are listed in Table S2.

(B) Genotyping of *Rbm8a* floxed mice. PCR using P3 and P4 generated a 872-bp band. After *Xho*I digestion, the loxp-containing product generated two bands of 594 bp and 318 bp, respectively. PCR using P5 and P6 generated a 220-bp band in the wild-type and a 260-bp band in the loxp-containing allele. PCR using P1 and P2 generated a 174-bp band in the wild-type and a 214-bp band in the loxp-containing allele.

(C) Immunoblotting shows Y14 and GAPDH proteins in E13.5 dorsal neocortex lysates with indicated genotypes.

(D) The brain of *Emx1*^{IREScre} and *Emx1*^{IREScre}*;Rbm8a*$^{f/+}$ at postnatal day 10.

(E) Immunofluorescence of E13.5 dorsal neocortices of *Emx1*^{IREScre} and *Emx1*^{IREScre}*;Rbm8a*$^{f/+}$ using antibodies against activated caspase 3 (CC3, green) and Tuj1 (red) and Hoechst staining (blue) were performed. CP, cortical plate; VZ, ventricular zone; SVZ, subventricular zone. Scale bar, 50 μm.

(F) Bar graph shows percentage of Pax6+ cells/total cells that were observed by immunostaining using anti-Pax6 and Hoechst staining as in panel G. The number of the cells (from three pairs of littermates) analyzed is indicated.

(G) Immunostaining and Hoechst staining of primary cells dissociated from the dorsal neocortices of *Emx1*^{IREScre} and *Emx1*^{IREScre}*;Rbm8a*$^{f/+}$ embryos. Upper and lower representative images show immunostaining of Pax6/γH2AX and Pax6/CC3, respectively; all were merged with Hoechst staining. Arrows and arrowheads depict Pax6-expressing cells without or with γH2AX (upper) or CC3 (lower), respectively. Scale bar, 25 μm.

Figure S3. Depletion of Y14 Causes DNA Damage and Sensitizes Cells to IR-induced Apoptosis. (Related to Figure 2).

(A) The neutral comet assay was performed in Y14-depleted MCF7 and U2OS cells. The comet tail was barely detected in the latter.

(B) siC or siY14-transfected HeLa and U2OS cells were exposed to increasing doses of IR followed by Clonogenic assay as in Figure 2B. Curve graphs show relative percentage of cell survival after different doses of IR. For each transfectant, the number of survived cells after IR was normalized to that of mock-treated cells. Mean ± SD were obtained from three independent experiments.

(C) The neutral comet assay was performed in siC, siY14 or eIF4A3-depleted HeLa cells.

Figure S4. Y14 Depletion Compromises the Expression of DDR Factors in Various Cell Lines. (Related to Figure 2).

(A) Immunoblotting of siC or siY14-transfected MCF7 and U2OS cell lysates was performed using antibodies against indicated proteins.
(B) Immunoblotting of siC, siY14 or sieIF4A3-transfected HeLa cell lysates.

Figure S5. Y14 Depletion-induced Transcription-dependent R-loops. (Related to Figure 2).
(A) Immunofluorescence detection of R-loops using antibody S9.6 in Y14-depleted MCF7 and U2OS cells. Scale bar in all cell images, 10 μm.
(B) Genomic DNA of siRNA-transfected HeLa cells was either left untreated or treated with RNase H and subjected to dot blot analysis using S9.6. Bar graph shows fold changes (mean ± SD) of S9.6 signals (non-RNase H treated siC was set as 1).
(C) siC or siY14-transfected HeLa cells were treated with 4 μM actinomycin D for 4 hrs, followed by immunofluorescence using antibody S9.6.
(D) HeLa cells were co-transfected with siC or siY14 and pcDNA3-RNase H1. Immunofluorescence was performed using anti-γH2AX and anti-RNase H1. siY14/RNase H-expressing cells (arrowhead) exhibited reduced γH2AX signals.
(E) DRIP using S9.6 was performed with siRNA-transfected HeLa cell lysates. Precipitates were mock treated or treated with RNase H, followed by qPCR using gene specific primers. For each DRIP, the precipitation efficiency (IP/input) was measured. Bar graph represents relative fold-enrichment (mean ± SEM) of the DNA-RNA hybrid for each gene (IgG was set as 1). *p*-values: * < 0.01, ** < 0.05, *** <0.001.
(F) Immunofluorescence of eIF4A3-depleted HeLa cells was performed as panel A.

Figure S6. Y14 Associates with Chromatin and its Phosphorylation is Abolished by ATM Inhibition. (Related to Figure 3).
(A) HEK293 cells were transfected with the empty vector or vector encoding FLAG-tagged Y14, eIF4A3, TAP or Upf3b. Immunoprecipitation using anti-FLAG was performed followed by immunoblotting.
(B) HEK293 cells were transfected with the empty or FLAG-Y14 vector, and exposed to 10 Gy IR. The lysates were mock-treated or treated with RNase, followed by immunoprecipitation and immunoblotting.
(C) HEK293 cells were transfected with siC or siATM and the empty or FLAG-Y14 vector. The cell lysates were subjected to immunoprecipitation using anti-FLAG, followed by immunoblotting.
(D) HEK293 cells were transiently transfected with the empty or FLAG-Y14 vector, and then mock-treated or treated with caffeine or KU55933. The cell lysates were analyzed by electrophoresis on a phosphate-affinity gel, followed by immunoblotting using anti-FLAG. **, hyperphosphorylated Y14; *, hypophosphorylated Y14.

Figure S7. Subnuclear Fractionation Reveals Chromatin-Associated Y14 prior to or post-DNA Damage. (Related to Figure 4).
(A) Immunoblotting of the whole cell extract (WCE) and RNase-treated (+) and non-treated (-) chromatin fractions (CSK) of MCF and HEK293 cells.
(B) Diagram shows RNA-mediated association of Y14 and Ku. After RNase treatment, only Y14 remained bound to chromatin. After DNA damage, chromatin localization of both proteins was enhanced and became RNase resistant.

(C) HeLa cells were mock-treated (-) or treated with phleomycin followed by recovery for 0, 1 or 2 hrs. Immunoblotting of the WCE and CSK+R fraction was performed using antibodies against indicated proteins.

Figure S8. Depletion of eIF4A3 Does Not Significantly Enhance Ku Retention on Chromatin. (Related to Figure 4).
HeLa cells were transfected with sieIF4A3, followed by phleomycin treatment, chromatin fractionation, and immunoblotting, as in Figure 6A. Bar graph shows the relative level of chromatin-bound Ku70 (left) and Ku80 (right) in siC and sieIF4A3 cells (lane 7 was set as 1).

Figure S9. Y14 Depletion Impairs DNA Repair in HeLa Cells. (Related to Figure 6).
(A) The end-joining assay was performed in HeLa cells. The uncut or cut (*Hind*III or I-*Sce*I) NHEJ reporter was co-transfected with siRNA (control, Y14, eIF4A3 or Ku80) into HeLa cells. Bar graphs show relative end-joining efficiency. Immunoblotting and PCR of GFP were performed as in Figure 6C-E. Asterisk indicates FLAG-Y14. *p*-values: * < 0.01, *** <0.001.
(B) The assay was performed as in panel A, except that cells were transfected with the indicated expression vector (empty, FLAG-Y14 or FLAG-Y14SA). *p*-values: * < 0.01, *** <0.001.

Transparent Methods

Cell Culture, Transfection and Drug Treatment

Culture and transient transfection of HeLa, HEK293, MCF7 and U2OS cells were carried out essentially as described (Chuang et al., 2013). U2OS stable cells containing a homology-directed repair (HDR) reporter (DR-GFP) were a kind gift of J. M. Stark and cultured as described (Gunn et al., 2011). Cells were, in general, collected 48 h after transfection with a siRNA or expression vector. Three siRNAs used including siY14, sieIF4A3 and negative control LO GC (Invitrogen) were previously describe (Lu et al., 2017). For DNA damage induction, cells were irradiated with various doses of X-rays or treated with 500 μM phleomycin (InvivoGen). For pharmacological treatment, cells were treated with actinomycin D (4 μM, Sigma-Aldrich) for 4 hrs, ATM inhibitor KU55933 (10 μM; Tocris) for 1 h prior to IR, caffeine (2 mM; Sigma) for 24 h or 5,6-dichloro-1-β-D-ribofuranosylbenzimidazole (DRB) (100 μM; Sigma) for 3 h prior cell harvest.

Plasmids and siRNAs

The expression vectors encoding FLAG-tagged Y14, Y14-SA and eIF4A3 and HA-tagged ubiquitin were previously described (Hsu Ia et al., 2005; Chuang et al., 2013; Lu et al., 2017). The pLKO.1-shY14-mCherry vector was constructed by replacing the puromycin sequence of pLKO.1-shY14 (Academia Sinica RNAi Core, Taipei) with mCherry; the shY14 sequence was CCGGCGAGAGCATTCACAAACTGAACTCGAGTTCAGTTTGTGAATGCTCTCGTTTTTG). The NHEJ reporter GFP-Pem1-Ad2 was a kind gift of Vera Gorbunova (University of Rochester (Seluanov et al., 2004). The I-*Sce*I expression vector pCB-ASce was obtained from Jeremy M. Stark (Beckman Research Institute of City of Hope, Duarte; (Gunn et al., 2011). The pEGFP-C1-FLAG-Ku70 was purchased from Addgene. The pcDNA3-RNase H1 was a kind gift from Andres Anguilera (Universidad de Sevilla, Servilla)(Bhatia et al., 2014). The GST-TAP and GST-Upf3b expression vectors were described (Chuang et al., 2011). siRNA targeting ATM was 5'-AGUCUAGUACUUAAUGAUCUGCUUA-3' (Invitrogen).

Conditional Knockout of *Rbm8a* in Mice

The two *loxp* sequences were inserted into intron 1 and the 3' end of *Rbm8a* using CRISPR/Cas9 to generate *Rbm8a* conditional allele. The guide RNA sequences used are 5'-GATAGTCTAGGAAACGCGAC and 5'- CCACCACTACACAGTGGTTT, respectively. The 5' (5'-gaagcaacaaaaataagagtcatttgaaaaaaaaaacaaaaaaaacctgtcCTCGAGATAACTTCGTATAATGTATGCTATACGAAGTTATgcgtttcctagactatctggaagcttcgacacagactccagcttcagtcccttcccagttccgccctaattcctttcccaaggggggaggagtctatcttttcagaccc) and 3' (5'-gatagtatataaacatacatgcaggcaaaaacctcattagatatttaaaccaaaaCTCGAGATAACTTCGTATAATGTATGCTATACGAAGTTATccactgtgtagtggtggtgcatgcctttgataccagccttgggaggaagaggcaggtagatctttctttgtgagttccagaccagcctggagaaagaaagtgggg) single strand HDR templates containing the *loxp* sequence (upper class) and *Xho*I (upper class and underlined) site were synthesized by IDT (Integrated DNA Technologies). The T7 promoter sequence (5'-TTAATACGACTCACTATA) was added upstream of gRNA sequence and a partial tracrRNA sequence (5'- GTTTTAGAGCTAGAAATAGC) was added downstream of the gRNA sequence. The oligonucleotide was annealed with reverse tracrRNA (5'-

TTTAAAAGCACCGACTCGGTGCCACTTTTTCAAGTTGATAACGGACTAGCCTTATT TTAACTTGCTATTTCTAGCTCTAAAAC) and PCR amplified using Phusion DNA polymerase (Thermo-Fisher Scientific) according to the manufacture's instruction. The amplified product was purified using QIAquick PCR purification Kit (Qiagen) and served as *in vitro* transcription template. The sgRNA were synthesized using HiScribe™ T7 Quick High Yield RNA Synthesis Kit from NEB (NEB). Cas9 mRNA was synthesized using mMESSAGE mMACHINE T7 ULTRA Kit (Thermo-Fisher Scientific), purified using MEGAclear Transcription Clean-up kit (Thermo-Fisher Scientific) and eluted with the injection buffer containing 10 mM Tris-HCl (pH7.2) and 0.1mM EDTA. The quality and quantity of RNAs were analyzed using NanoDrop ND-1000 (Thermo-Fisher Scientific).

For mice production, the 5' *loxp* and 3' *loxp* were inserted by sequential injection of the 5'- and 3'-sgRNA along with Cas9 mRNA and single strand oligonucleotide (ssODN) independently. The 3'-*loxp*-*Xho*I HDR template was first inserted to generate 3'-*loxp* inserted mice. These mice were then used as breeder, and their zygotes were subjected to subsequent injection of 5'-*loxp*. For the injection, Cas9 mRNA, sgRNAs and ssODN were diluted with injection buffer to final concentration of 50, 50 and 100 ng/μl, respectively. Super-ovulated C57BL/6J female mice of 3-4 week old were set mating to male mice and one-cell stage zygotes were collected on the next day. The mixture of Cas9 mRNA, sgRNA and ssODN was injected into both pronuclei and cytoplasm of the zygotes. Injected zygotes were cultured in EmbryoMax KSOM Medium in humidified incubator (37^{o}C, 5% CO_2) for overnight. Two-cell stage embryos were transferred into the oviduct of 0.5-dpc pseudo-pregnant ICR female mice (BioLASCO, Taiwan).

To confirm the 3'-*loxp* knock-in, the 3' end region was PCR amplified using the following primer pair: P3 (5'- CCTCTTCCAGAGGTCCTAAGTCCAA) and P4 (5'- GTAGCAGCAATAGCCTGACTATAGTTGT). For 5'- and 3'-*loxp* knock-in, PCR primers P7 (5'- GAAGATTTCGCCATGGATGAGGATGG) and P4 were used to amplify the region comprising 5'- and 3'-loxp. The PCR product that can be digested with *Hind*III was further sequenced to confirm the two *loxp* sites that remained intact. After genotype confirmation, heterozygous mice (*Rbm8a*$^{f/+}$) were mated to *Emx1*^{IREScre} mice (Gorski et al., 2002) generously provided by Kevin R. Jones (University of Colorado, Boulder) to obtain *Emx1*^{IREScre};*Rbm8a*$^{f/+}$. The *Emx1*^{IREScre} littermates were used as control. The following were also used for genotyping: P1 (5'- CCTTGGGAAAGGAATTAGGGGC), P2 (5'- GTTTGTGGATGCTTTCTAGAGTTCCAG), P5 (5'- GATCTACCTGCCTCT TCCTCCCA) and P6 (5'- GACAGATTGAATCCCCCATCCACA).

All experimental procedures involving animals were approved by the Institutional Animal Care and Use Committee (IUCUC) 17-08-1104 of Academia Sinica and complied with the Ministry of Science and Technology, Taiwan.

Immunostaining and Isolation of Embryonic Brain Cells

The procedure for immunostaining of E13.5 mouse embryonic cortex is described in Supplemental Information. For immunostaining, polyclonal antibodies against γH2AX (Novus), Pax6 (BioLegend) and CC3 (Cell Signaling) and monoclonal antibodies against Y14 (Abcam), Pax6 (DSHB) and Tuj1 (Biolegend) were used. Secondary antibodies used were conjugated with Alexa Fluor 488 (green) or Alexa Fluor 568 (red). To collect primary brain cells, E13.5 embryonic dorsal cortices were dissected and dissociated according to (Mao et al., 2015). Isolated cells were plated on poly-D-lysine-coated coverslips in 6-well

culture dishes and incubated in DMEM-F12 medium supplemented with N2, Glutamax, Non-Essential Amino Acids (NEAA), bFGF, EGF, penicillin-streptomycin, and amphotericin (all from Gibco) at 37°C for 3 h. Attached cells were fixed with 4% paraformaldehyde for 10 min for indirect immunofluorescence and staining with Hoechst.

Neurosphere Formation
Primary brain cells were isolated and incubated in the same medium described as above. Dissociated cells were cultured in Ultra-Low attachment surface plate (Corning) for 10 days. Neurosphere area was measured by Image J.

Colony Formation Assay
siRNA-transfected cells were cultured for 3 weeks and colonies were fixed and stained as described in (Lai et al., 2010).

Neutral Comet Assay
The procedure is described in (Nowsheen et al., 2012). Briefly, after harvest, cells were suspended in 1% low-melting agarose (Sigma) at 10^5 cells/ml and embedded on slides, followed by treatment with cold lysis buffer (2.5 M NaCl, 100 mM EDTA, 10 mM Tris base, 1% sodium lauryl sarcosinate, 1% TritonX-100, pH 10). The slides were subjected to electrophoresis using 1 V/cm for 15 min at 4˚C. After electrophoresis, slides were fixed with ethanol and stained with SYBR green. Images were acquired by using Zeiss confocal 700 microscope, and the tail moment was analyzed using CASP software (CaspLab).

Chromatin Fractionation
The procedure for chromatin fractionation is described in (Britton et al., 2013). Essentially, cells were washed twice with phosphate-buffered saline and then incubated at 4˚C for 3 min in the cytoskeleton (CSK) buffer containing 10 mM PIPES (pH 7.0), 100 mM NaCl, 300 mM sucrose, 3 mM $MgCl_2$, and 0.7% Triton X-100 and optionally supplemented with 0.3 mg/ml RNase A. After centrifugation at 5000×*g* for 3 min, the chromatin-enriched pellet was washed three times with phosphate-buffered saline containing protease inhibitors, and collected in the SDS lysis buffer.

Immunoprecipitation and Mass Spectrometry
The procedure for immunoprecipitation-mass spectrometry was carried out essentially as previously described (Lee and Tarn, 2014). In brief, approximately 1.5×10^7 HEK293 cells were transiently transfected with 20 μg of pCDNA-FLAG-Y14. The cell lysate was prepared and subjected to immunoprecipitation using anti-FLAG M2 affinity gel (Sigma). For mass spectrometry, immunoprecipitates were fractionated on SDS-polyacrylamide gels and stained with SYPRO-Ruby (Bio-Rad). The bands of interest were excised, trypsinized and subjected to liquid chromatography coupled with tandem mass spectrometry (LTQ XL, ThermoFinnigan). For the analysis of mass spectrometry data, the Voyager-DE STR Biospectrometry Workstation (Applied Biosystems) and Mascot software (www.matrixscience.com) were used. Polyclonal anti-Y14 (Bethyl) and anti-Ku80 (Cell Signaling Technology) were used for immunoprecipitation of endogenous Y14 and Ku. Rabbit IgG (Bethyl) was used as control.

Immunoblotting
Immunoblotting was performed according to Chuang et al. (2013). Monoclonal antibodies used were against RNA pol II C-terminal domain (CTD) (Abcam), ATM, Mre11, and Nbs1 (Genetex), Chk1 (Santa Cruz Biotechnology), Chk2 (MBL), GAPDH (ProteinTech) and α-tubulin (NeoMarkers). Polyclonal antibodies used were against FLAG epitope (Sigma), HA epitope (Bioman), Y14, MDC1, XLF, Trim28 (Bethyl), γH2AX, 53BP1 (Novus), DNA ligase IV (Acris), XRCC4 (GeneTex), eIF4A3, p53 (ProteinTech), Magoh, DNA-PK, Rad51 (Abcam), histone 3, Ku70, Ku80, ATR, phospho-Chk1 and phospho-Chk2 (Cell Signaling Technology).

Immunofluorescence
Immunofluorescence was performed essentially as described (Chuang et al., 2013). Polyclonal primary antibodies used were against Y14 (Bethyl), eIF4A3 (ProteinTech), CC3 (Cell Signaling) and 53BP1 (Novus), and monoclonal antibodies were against γH2AX (Millipore) and Y14 (Abcam). Secondary antibodies were conjugated with FITC or rhodamine (anti-mouse or anti-rabbit IgG, Cappel). Nuclei were counterstained with Hoechst 33258 or DAPI. The specimens were observed using a laser-scanning confocal microscope (LSM 780, Carl Zeiss) coupled with an image analysis system. To detect R-loops, cells were fixed in ice-cold methanol for 20 min, followed by hybridization overnight with antibody S9.6 (ENH001, Kerafast) and subsequently with FITC-conjugated anti-mouse IgG for 2 h. Visualization was performed using a laser-scanning microscope (LSM 700, Carl Zeiss).

Laser Microirradiation and Live-cell Imaging
The cDNAs encoding Ku70 and Ku80 were fused with the EGFP cDNA, cloned into a retrovirus vector pLNCX (Clontech), and used to transduce U2OS cells as described (Pan et al., 2015). U2OS cells stably expressing GFP-fused MDC1 were from a previous study (Chang et al., 2015). Cells were mounted onto the incubation stage in a SP5 X inverted confocal microscope (Leica Microsystems) supplemented with humidified 5% CO_2 at 37 °C. Laser-microirradiation was carried out using a laser diode (405 nm) with full output settings. Ten scans were applied to generate DNA damages restricted to the laser path with minimal cellular toxicity. Live-cell images were taken every 15 s using the same confocal microscope with the minimum-detectable output of a laser diode (488 nm). Fluorescence intensity was measured with ImageJ (National Institutes of Health, USA).

***In Vitro* Pull-down Assay**
Recombinant GST-Y14 fusion proteins (full-length, ΔN lacking the N-terminal 55 amino acids and ΔC lacking the C terminal 23 amino acids) have been previously described (Hsu Ia et al., 2005; Chuang et al., 2013). Phosphorylated Y14 was obtained by co-expression of SR protein kinase 1 and GST-Y14 in bacteria (Hsu Ia et al., 2005). For the *in vitro* pull down assay (Hsu Ia et al., 2005), 5 μg of GST or GST-Y14 (full-length, truncated or phosphorylated forms) was incubated with 50 μg of HeLa cell lysates. After extensive wash, bound proteins were analyzed by immunoblotting.

End-joining Assay

The procedure for the end-joining assay was as described (Seluanov et al., 2004). In brief, the NHEJ reporter was digested with *Hind*III or I-*Sce*I. U2OS cells were co-transfected with uncut or linearized reporter and an siRNA. For the rescue experiment, the expression vector for siY14-resistant FLAG-Y14 was used for co-transfected. The number of GFP-positive cells was determined 48 h post-transfection by fluorescence-activated cell sorting using 17-color LSR II Analytic Flow Cytometer (BD Biosciences).

Immunostaining of Embryonic Brain

Immunostaining of E13.5 mouse embryonic cortex was essentially described in (Silver et al., 2010). In brief, brain slices were fixed overnight in 4% paraformaldehyde at 4°C, followed by submersion in 30% sucrose. Brain cryostat sections were permeabilized with 0.2% Triton X-100 for 10 min, blocked with MOM block reagent (Vector Laboratories) for 1 h at room temperature, and incubated with appropriate antibodies (indicated in the text) overnight at 4°C. Finally, sections were incubated with an appropriate secondary antibody and stained with Hoechst 33258 (Sigma).

Dot Blot R-loop Assay

Genomic DNA was extracted from cells and subsequently treated (or not treated) with 50 U/ml RNase H (New England Biolabs). For assay, 100 ng of DNA was spotted onto a nitrocellulose membrane. The membrane was incubated with antibody S9.6 overnight, followed by incubation for 1 h with horseradish peroxidase-conjugated goat anti-mouse IgG (Santa Cruz Biotechnology). Signals were detected using the SuperSignal West Pico Chemiluminescent substrate (Thermo Fisher Scientific), and images were acquired using FlourChemQ (Protein Simple).

Immunoprecipitation of DNA-RNA Hybrids

DRIP was performed essentially according to Halasz et al. (Halasz et al., 2017). For each transfection, 6 µg of sonicated genomic DNA was incubated with 3-µg S9.6-conjugated protein A beads (10 µl) in the immunoprecipitation buffer (50 mM HEPES pH 7.5, 140 mM NaCl, 5 mM EDTA, 1% Triton X-100 and 0.1 % deoxycholate) at 4°C for 3 h. For RNase H treatment, the beads were incubated with 50 U RNase H (New England Biolabs) at 37˚C for 2.5 h; 10 mM EDTA was added to stop the reaction. Beads were washed extensively with the immunoprecipitation buffer and twice with 10 mM Tris-HCl (pH 8). DNA-RNA hybrids were eluted with a buffer containing 100 mM $NaHCO_3$ and 1% SDS for 10 min at 37˚C followed by phenol-chloroform extraction. qPCR was performed using specific primers (Table S2) with LightCycler 480 SYBR Green I Master (Roche) and analyzed with a QuantStudio 12K Flex Real-Time PCR System (Thermo Fisher Scientific).

Phosphate-Affinity Gel Electrophoresis

HEK293 cells were transfected with the vector encoding FLAG-Y14 or its non-phosphorylatable mutant. Cell lysate was fractionated on Phos-tag™ Acrylamide gel according to manufacturer’s instruction (Wako).

Statistical Analysis

Statistical analysis was performed using GraphPad Prism 7.0.

Supplemental References

Bhatia, V., Barroso, S.I., Garcia-Rubio, M.L., Tumini, E., Herrera-Moyano, E., and Aguilera, A. (2014). BRCA2 prevents R-loop accumulation and associates with TREX-2 mRNA export factor PCID2. Nature *511*, 362-365.

Britton, S., Coates, J., and Jackson, S.P. (2013). A new method for high-resolution imaging of Ku foci to decipher mechanisms of DNA double-strand break repair. J Cell Biol *202*, 579-595.

Chang, C.F., Chu, P.C., Wu, P.Y., Yu, M.Y., Lee, J.Y., Tsai, M.D., and Chang, M.S. (2015). PHRF1 promotes genome integrity by modulating non-homologous end-joining. Cell Death Dis *6*, e1716.

Chuang, T.W., Chang, W.L., Lee, K.M., and Tarn, W.Y. (2013). The RNA-binding protein Y14 inhibits mRNA decapping and modulates processing body formation. Mol Biol Cell *24*, 1-13.

Chuang, T.W., Peng, P.J., and Tarn, W.Y. (2011). The exon junction complex component Y14 modulates the activity of the methylosome in biogenesis of spliceosomal small nuclear ribonucleoproteins. J Biol Chem *286*, 8722-8728.

Gorski, J.A., Talley, T., Qiu, M., Puelles, L., Rubenstein, J.L., and Jones, K.R. (2002). Cortical excitatory neurons and glia, but not GABAergic neurons, are produced in the Emx1-expressing lineage. J Neurosci *22*, 6309-6314.

Gunn, A., Bennardo, N., Cheng, A., and Stark, J.M. (2011). Correct end use during end joining of multiple chromosomal double strand breaks is influenced by repair protein RAD50, DNA-dependent protein kinase DNA-PKcs, and transcription context. J Biol Chem *286*, 42470-42482.

Halasz, L., Karanyi, Z., Boros-Olah, B., Kuik-Rozsa, T., Sipos, E., Nagy, E., Mosolygo, L.A., Mazlo, A., Rajnavolgyi, E., Halmos, G., *et al.* (2017). RNA-DNA hybrid (R-loop) immunoprecipitation mapping: an analytical workflow to evaluate inherent biases. Genome Res *27*, 1063-1073.

Hsu Ia, W., Hsu, M., Li, C., Chuang, T.W., Lin, R.I., and Tarn, W.Y. (2005). Phosphorylation of Y14 modulates its interaction with proteins involved in mRNA metabolism and influences its methylation. J Biol Chem *280*, 34507-34512.

Lai, M.C., Chang, W.C., Shieh, S.Y., and Tarn, W.Y. (2010). DDX3 regulates cell growth through translational control of cyclin E1. Mol Cell Biol *30*, 5444-5453.

Lee, K.M., and Tarn, W.Y. (2014). TRAP150 activates splicing in composite terminal exons. Nucleic Acids Res *42*, 12822-12832.

Lu, C.C., Lee, C.C., Tseng, C.T., and Tarn, W.Y. (2017). Y14 governs p53 expression and modulates DNA damage sensitivity. Sci Rep *7*, 45558.

Mao, H., Pilaz, L.J., McMahon, J.J., Golzio, C., Wu, D., Shi, L., Katsanis, N., and Silver, D.L. (2015). Rbm8a haploinsufficiency disrupts embryonic cortical development resulting in microcephaly. J Neurosci *35*, 7003-7018.

Nowsheen, S., Xia, F., and Yang, E.S. (2012). Assaying DNA damage in hippocampal neurons using the comet assay. J Vis Exp, e50049.

Pan, W.A., Tsai, H.Y., Wang, S.C., Hsiao, M., Wu, P.Y., and Tsai, M.D. (2015). The RNA recognition motif of NIFK is required for rRNA maturation during cell cycle progression. RNA Biol *12*, 255-267.

Seluanov, A., Mittelman, D., Pereira-Smith, O.M., Wilson, J.H., and Gorbunova, V. (2004). DNA end joining becomes less efficient and more error-prone during cellular senescence. Proc Natl Acad Sci U S A *101*, 7624-7629.
Silver, D.L., Watkins-Chow, D.E., Schreck, K.C., Pierfelice, T.J., Larson, D.M., Burnetti, A.J., Liaw, H.J., Myung, K., Walsh, C.A., Gaiano, N., *et al.* (2010). The exon junction complex component Magoh controls brain size by regulating neural stem cell division. Nat Neurosci *13*, 551-558.